




RESEARCH ARTICLE | MAY 02 2023

Ventilated cavity dynamics of an axisymmetric body under the influence of a structure

Special Collection: [Cavitation](#)

Zhang Di (张迪) ; Zhang Jianyu (张健宇); Sun Tiezhi (孙铁志)  ; Jiang Yichen (姜宜辰)

 Check for updates

Physics of Fluids 35, 055112 (2023)

<https://doi.org/10.1063/5.0147279>



CrossMark



Biomicrofluidics

Special Topic: Microfluidic Biosensors

Submit Today



Ventilated cavity dynamics of an axisymmetric body under the influence of a structure

Cite as: Phys. Fluids **35**, 055112 (2023); doi: [10.1063/5.0147279](https://doi.org/10.1063/5.0147279)

Submitted: 21 February 2023 · Accepted: 13 April 2023 ·

Published Online: 2 May 2023



View Online



Export Citation



CrossMark

Di Zhang (张迪),¹  Jianyu Zhang (张健宇),^{1,2} Tiezhi Sun (孙铁志),^{1,a)}  and Yichen Jiang (姜宜辰)¹

AFFILIATIONS

¹School of Naval Architecture, State Key Laboratory of Structural Analysis, Optimization and CAE Software for Industrial Equipment, Dalian 116024, China

²Changchun Institute of Optics, Fine Mechanics and Physics, Chinese Academy of Sciences, Changchun 130033, China

Note: This paper is part of the special topic, Cavitation.

^{a)} Author to whom correspondence should be addressed: suntiezhi@dlut.edu.cn

ABSTRACT

The presence of structures in the ocean complicates the navigation of an underwater axisymmetric body. This effect involves special environmental fluid dynamics, such as unsteadiness, strong nonlinearity, cavity multiphase flow, strong turbulence, and so forth. In this paper, an improved delayed detached eddy simulation method is used to investigate the ventilated cavity flow of an axisymmetric body in the ocean, with the intent of exploring differences in cavity multiphase flow characteristics in the presence and absence of a structure. The presence of the structure advances the deflation of the tail, shortening the length of the main body of the ventilated cavity by 21.1%. In addition, the interference of the structure increases the shedding of multi-scale vortices, while the cavity body and the shedding vortices appear asymmetrical. Moreover, the existence of the structure increases the violence of the pressure fluctuation of the axisymmetric body, where the pressure fluctuation directly below the structure reaches 57.6%, and the fluctuation of the distribution probability of the cavitation number also increases. It is worth noting that the existence of the structure does not change the main frequency of the ventilated cavity shedding in front of the structure.

Published under an exclusive license by AIP Publishing. <https://doi.org/10.1063/5.0147279>

I. INTRODUCTION

The underwater launch of a vehicle must overcome complex flow problems, including cavity oscillation and the influence of the free surface and waves.^{1,2} As the vehicle approaches the mixture of ice and water in the polar region, the flow field changes more drastically than when it sails in the water alone. Therefore, it is of great significance to study the influence of structures on cavity dynamics for the navigation of vehicles in ice regions.

Cavitating flow has unsteady characteristics, such as multiphase flow, high turbulence, and multi-scale vortex flow.^{3,4} Many studies have researched this topic,^{5–9} and people have begun to use the cavity phenomenon. The potential of ventilated gas supercavitation in high-speed drag reduction and the facilitation of high-speed marine lifting surfaces have been confirmed by hydrodynamics.¹⁰ Ceccio¹¹ analyzed the problem and found that ventilation can make the surface of the vehicle model show the state of the gas–liquid mixture, so as to achieve the purpose of drag reduction. Zou *et al.*¹² used a self-developed numerical method to simulate the accelerating and decelerating motions of a vehicle in straight flight and discussed the motion

characteristics of the vehicle. The hydrodynamic performance of an underwater supercavitation vehicle is affected by the cavity morphology and closure mechanism. Karn *et al.*¹³ investigated the physical mechanisms that determine closure formation and transitions between different closure modes according to ventilated supercavities in a closed-wall recirculating water tunnel. Following this, Sun *et al.*^{14–16} observed three unsteady flow patterns and three distinct cavity regimes in water tunnel experiments and studied the effects of internal waves on supercavity closure and shedding periods. Their work laid the foundation for the further study of hydrodynamic characteristics and the motion stability of ventilated supercavitating vehicles in maneuvering states. To date, the study and development of underwater high-speed vehicles using supercavitation drag reduction have attracted much attention, and great development prospects remain.

The interaction between vehicles and structures is an important research topic in the field of ocean engineering. Studies of interactions between a ship and sea ice can provide an important reference for understanding the interaction between vehicles and structures.^{17–19} Many studies of ships moving in icy conditions have been conducted

recently, and the influence of structures on underwater vehicles requires further discussion. The motion of the vehicle^{20,21} and ice-breaking capacity^{22–24} under the ice have been well studied. For vehicles with ventilated cavitation, it is of great significance to study how structures interfere with cavitation. Blake *et al.*²⁵ conducted experiments and performed numerical calculations to explore the interactions between the motion of two vertical bubbles near a rigid wall and found that the strength of interaction between the bubbles was no less than that between a bubble and a rigid wall. Chan *et al.*²⁶ studied the complex interactions between bubbles and structures and found obvious differences in the gravitational effects between different jet bubbles. Using experimental methods, Cui *et al.*²⁷ studied the impact of the collapse of a pair of interacting bubbles on ice and analyzed ice-breaking abilities. The fluid–solid coupling between cavitation and the structure makes navigation more difficult than usual. Therefore, it is important to grasp the multiphase flow characteristics and load characteristics of an underwater vehicle.

Before a vehicle exits water, it must go through an underwater high-speed unsteady navigation stage. The natural cavitation or ventilated cavitation generated at this point forms a complex multiphase flow. It is necessary to capture the interface of the mixture to solve the cavity. The boundary element method,²⁸ the Logvinovich method,²⁹ arbitrary Lagrange–Euler (ALE)³¹ based on the Navier–Stokes equation are usually used for solving cavity. The volume of fluid (VOF)³⁰ method can be used to capture and track the interface. Then, in 2008, Passandideh–Fard and Roohi³² improved the VOF model and applied it to the simulation of the cavitation. Fronzo³³ proposed probability distribution functions (PDFs) to analyze the pressure distribution inside a cavity and improved the understanding of unsteady ventilated cavitation flows. The numerical results were in good agreement with those of the experimental and analytical relationships. Gui *et al.*,³⁴ studying vortices, compared the Ω method with other methods of vortex identification by studying vortex structure in a flow field of a rotating jet and found that the Ω method can show more secondary weak vortex structures at the same time. The current understanding of the interactions between a ventilated cavity and structures is insufficient. Analyzing the results from multiple perspectives is helpful to fully understand the evolution of its complex flow field.

A detached eddy simulation (DES) method is used in this work, and the results are compared with the experimental data for verification. Using a proven numerical method, we explore the effects of a structure on ventilated cavity flows. Due to the complexity of the navigation process in the ice area of the vehicle, we made the following assumptions, aiming to focus on the physical problems involved: (1) The structure is regarded as a low-temperature rigid body near the vehicle and ignore the relative motion between them and (2) ignore the heat transfer and phase change during navigation. The remainder of this article is organized as follows: Section II introduces the control equations and numerical models, as well as the experimental comparison and verification of numerical methods. Section III presents the results of the numerical simulation. We first discuss the influence of a structure near the axisymmetric body on the evolution characteristics of the cavity and vortex structures. Then, PDFs are used to analyze the distribution probability of the cavitation number during the development and stability of the cavity. The time and space characteristics of the load on the axisymmetric body are explored at this point as well. Finally, the main findings are summarized in Sec. IV.

II. NUMERICAL METHOD

A. Governing equations

The numerical simulations in this article involve multiple incompressible flows. In the research of computational fluid dynamics (CFD), a fluid is considered a continuous medium, that is, it satisfies the continuity equation,

$$\nabla \bullet (\rho_m \mathbf{u}) = 0, \tag{1}$$

where $\nabla = \frac{\partial}{\partial x} i + \frac{\partial}{\partial y} j + \frac{\partial}{\partial z} k$ is called the Hamiltonian, ρ_m is the density of the mixed fluid, and \mathbf{u} is the speed of the continuum.

The equation for the conservation of momentum is

$$\frac{\partial(\rho_m \mathbf{u})}{\partial t} + \nabla \bullet (\rho_m \mathbf{u} \otimes \mathbf{u}^T) = -\nabla p + \nabla \bullet [\mu_m (\nabla \mathbf{u} + \nabla \mathbf{u}^T)] + \mathbf{F}_b. \tag{2}$$

Among these, t represents the time, \otimes denotes the outer product, μ_m is the dynamic viscosity of the mixed fluid, \mathbf{F}_b is the resultant force of various volume forces acting on the continuum, and p is the pressure.

The density of the mixed phase ρ_m is the weighted average of the density of each phase,

$$\rho_m = \rho_l \alpha_l + \rho_g \alpha_g, \tag{3}$$

where ρ represents the density of each phase fluid, α represents the volume fraction of each fluid, and the subscripts m, l, g represent the mixed phase, liquid phase, and gas phase, respectively.

In this work, the VOF multiphase model is used to capture the interface between bubble and gas and predict the distribution and movement of the interface of the immiscible intersection. The phase distribution and position of the interface are expressed by the field of the phase volume fraction α_n . The volume fraction of phase n is defined as follows:

$$\alpha_n = \frac{V_n}{V}, \tag{4}$$

where V_n is the volume of n in the grid cell, and V is the volume of the grid cell.

The sum of the volume fraction of each item is 1,

$$\alpha_l + \alpha_g = 1. \tag{5}$$

According to the volume fraction, the existence of different kinds of phases or fluids can be distinguished.

B. Detached eddy simulation method

Detached eddy simulation (DES) is a hybrid modeling method that combines the Reynolds average simulation (RANS) characteristics of some parts of the fluid with the large eddy simulation (LES) characteristics of other parts of the fluid. The improved delayed detached eddy simulation (IDDES) method of shear stress transfer (SST) K-Omega used in this paper introduces the wall-modeled LES method that establishes the relationship between the subgrid length and the wall distance.³⁵ The RANS method was used to solve for the boundary layer and irrotational regions, and the LES method was used to simulate the separated flow regions in the flow field.^{36,37} We replace the

dissipation term $\tilde{\omega}$ in the original SST K-Omega turbulent kinetic energy transfer equation with ω ,

$$\omega = \frac{\sqrt{k}}{l_H f_{\beta^*} \beta^*}, \tag{6}$$

where k is the kinetic energy of the continuum, f_{β^*} is the free shear correction factor, and $\beta^* = 0.09$ is the model coefficient,

$$l_H = f_d(1 + f_e)l_{RANS} + (1 - f_d)C_{DES}\Delta_{IDDES}, \tag{7}$$

where $C_{DES} = 0.78$, and l_{RANS} is the length scale of RANS. The IDDES method introduces the two functions f_d and f_e to modify the mixed length scale and control the conversion from RANS to LES. In addition,

$$\Delta_{IDDES} = \min(\max(0.15d, 0.15\Delta, \Delta_{\min}), \Delta), \tag{8}$$

where d is the distance to the wall, Δ is the maximum distance between the grid cell center and the grid cell center of the adjacent grid cell, and Δ_{\min} is the minimum distance between the grid cell center and the grid cell center of the adjacent grid cell.

Then, the turbulent kinetic energy equation can be written as follows:

$$\begin{aligned} \frac{\partial(\rho_m \omega)}{\partial t} + \nabla \cdot (\rho_m \omega \bar{\mathbf{u}}) &= \nabla \cdot [(\mu_m + \sigma_\omega \rho_m k T) \nabla \omega] + P_\omega \\ &- \rho_m \beta f_\beta (\omega^2 - \omega_0^2) + S_\omega, \end{aligned} \tag{9}$$

where $\bar{\mathbf{u}}$ is the average speed, $\sigma_\omega = 0.5$ is the model coefficient, T is the turbulence timescale, P_ω is the resulting item, f_β is the eddy current extension correction factor, S_ω is a user-specified source item, and ω_0 is the ambient turbulence value that prevents turbulence decay.

C. Numerical setup

Figure 1 shows the geometry of the axisymmetric body and the structure, as well as the dimensional parameters. The model includes a conical shape head that is 30 mm long and 50 mm across, with a cylindrical body that is 320 mm long and 50 mm across, for a total length of 350 mm. At the junction of the head, the body is a 3-mm-wide ventilation port that is used to ventilate the supercavity. The structure is $20 \times 20 \times 10 \text{ mm}^3$. To monitor pressure fluctuation during the evolution of the cavity, four pressure monitoring points (P1, P2, P3, and P4) are installed on the side of the model surface close to the structure. P1 is 25 mm from the head of the model, and the distance between P1 and P2 is 13 mm. P3 is located 18 mm directly below the center of the structure at 7 mm from P2, and P4 is 25 mm to the right of P3.

Figure 2 shows a schematic diagram of the computational domain. The diameter of the axisymmetric body is $D = 50 \text{ mm}$. The distance between the inlet and the front of the axisymmetric body is $24D$, and the outlet is $20D$ downstream of the body. The cross section along the axis of the computational domain is a square with a side length of $16D$. The entrance to the computational domain is set to a velocity inlet of $U_\infty = 10 \text{ m/s}$, and the four surroundings are set as symmetry planes, with the outlet assigned as pressure outlet. The environmental pressure of the domain is 0.103 MPa . In addition, $C_Q = \frac{Q}{U_\infty D^2} = 0.34$ is equivalent to the rate that air escapes the supercavity, where Q is the value of the gas volume flow rate.

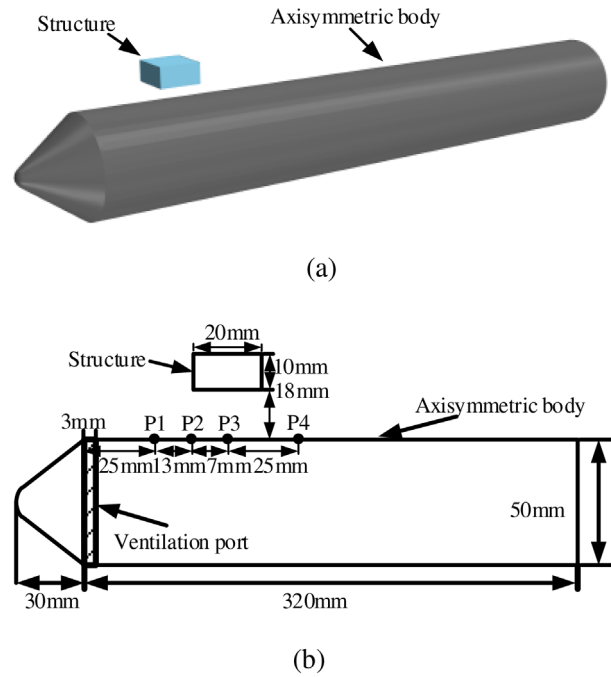


FIG. 1. Diagram of the computational domain: (a) numerical calculation model and (b) dimensional parameter.

The method of mesh refinement is indicated in Fig. 3. The computational mesh was created using the Star-CCM+ trimmed mesh generator, which provides a stable and efficient method to generate high-quality meshes for both simple and complex models and can accurately predict cavity multiphase and separation flows. There is a refinement for the upstream zone and the surface of the axisymmetric body. To improve the gas capture, the mesh of the ventilation port has been refined more finely. The mesh is approximately 4.5×10^7 cells. There is a prism layer near the axisymmetric body and the structure that meets the rule of $y^+ < 1$. Considering the good transition between the near-wall inflation layer mesh and the wall-parallel mesh, the growth rate of near-wall inflation layer is selected as 1.5. When the Courant number is 1, the solution time step is $1 \times 10^{-4} \text{ s}$.

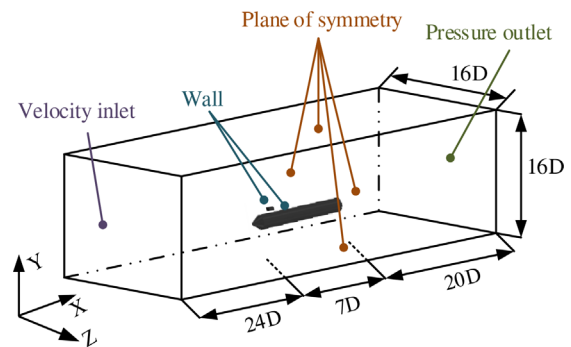


FIG. 2. Calculation domain and boundary condition.

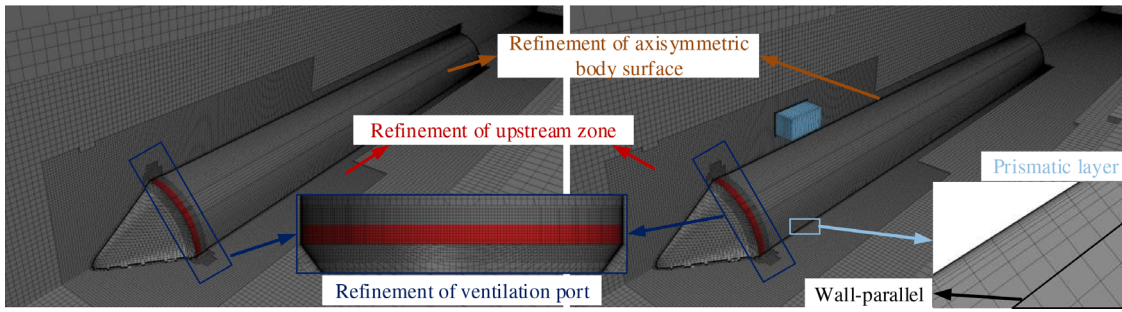


FIG. 3. Computational model three-dimensional meshing.

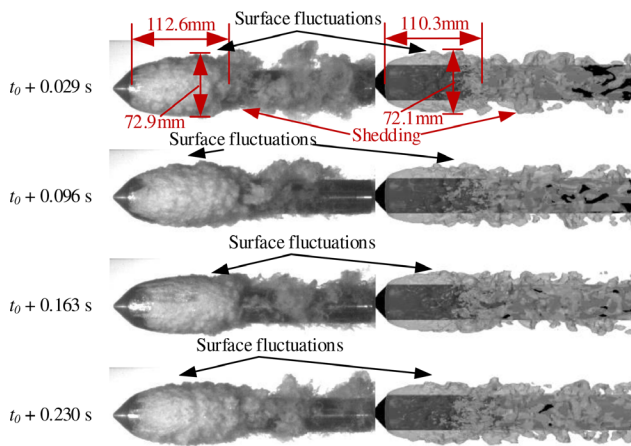


FIG. 4. The cavity shape of the experiment is compared to numerical simulation.

D. Numerical methods validation

Model validation was conducted through experiments performed in the high-speed water tunnel at Harbin Institute of Technology, Harbin, China. This experimental system has been described in detail

in a previous article.³⁸ In this experiment, the test model is 274 mm long, 0.04 m in diameter, and 1 mm wide at the ventilation port. The working pressure was 68.4 kPa, the flow velocity of the water tunnel is 10.21 m/s, and Q in the experiment is 129 l/min, giving a ventilation flow rate of $C_Q = 0.17$ and a flow velocity of 8.07 m/s. All of the parameters in the numerical simulation are set in accordance with the experiment. The right side of Fig. 4 shows the iso-surface with a water volume fraction of 0.5 in the four cycles of the simulation. Comparing it with the experimental picture on the left, it can be seen that the two cavities are in good agreement. In the experiment, the length of the transparent cavity is 112.6 mm, while the length of the transparent cavity in the numerical simulation is 110.3 mm. The diameters of the transparent cavity in the experiment and numerical simulation are 72.9 and 72.1 mm, respectively. Behind it are cloudy cloud cavities, and they begin to shed. At the same time, the numerical simulation also captures the surface fluctuations in the experiment at the same position of the cavity.

Figure 5 provides a comparison of pressure fluctuation in the cavity and at the tail of the model. The numerical prediction results are generally consistent with the experimental data. Among them, the average values of the absolute pressure measured by the experiment and numerical simulation at P_{E1} are 52.3 and 52.9 kPa, respectively. The average values of pressure measured by the experiment and

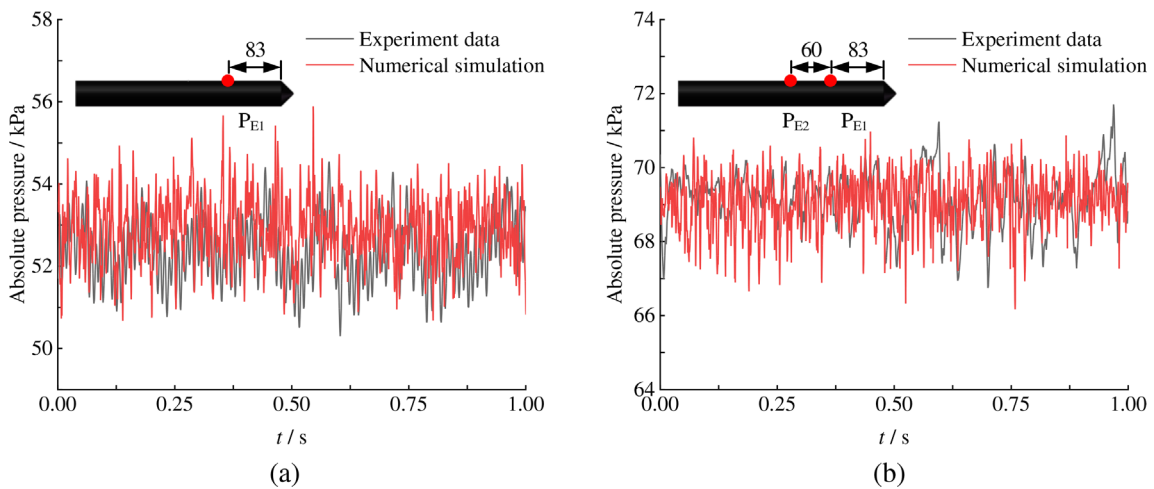


FIG. 5. Analysis of pressure comparison: (a) pressure comparison in the cavity and (b) comparison of the pressure at the tail of the model.

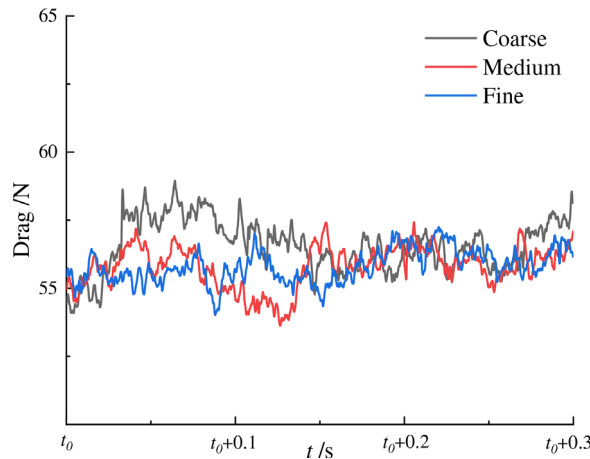


FIG. 6. Drag with different mesh numbers.

numerical simulation at P_{E2} are 69.1 and 69.1 kPa, respectively. Therefore, the numerical methods mentioned can effectively simulate ventilated cavities.

Zhou *et al.*³⁹ studied the difference of ventilated supercavitating flows between water tunnel experiments. Cao *et al.*⁴⁰ also conducted experiments on the effect of blockage ratio on ventilation cavity. The results found that the normalized shapes of 5% and 9% blockage ratio were similar. The blockage ratio of this work is 6.25%, and the influence of the wall effect on the calculation can be ignored. Choe and Kim⁴¹ used the trimmed mesh to predict the cavity shapes around a high-speed underwater vehicle and captured substantial nonlinear characteristics, such as lift, drag, and pitching moment, which shows that the trimmed mesh has a wide application in the calculation of ventilated supercavitating flows. Therefore, in this study, the following mesh numbers were verified based on the DES model and the trimmed mesh.

Figure 6 and Table I show the mesh independent analysis of this numerical simulation method. With the increase in the number of meshes, the drag of the vehicle exhibits a convergence trend. In addition, the fluctuations of the medium mesh size and the fine mesh size also have good consistency. Considering the calculation efficiency and accuracy, the medium mesh size is used in this paper.

In the present study, an unsteady ventilated cavity of an axisymmetric body under the influence of structures is solved using the finite volume method of STAR-CCM+. The numerical scheme is formally second-order accurate in space and time. To balance accuracy and efficiency, according to the setting of the relevant research,^{42–44} the number of inner iterations for each time step is 5, and the final convergence criterion is 1×10^{-3} . The interface between water and air is solved with the VOF model, using a second-order implicit scheme. At this time, high-resolution interface capture (HRIC) is used to simulate the convective transport of immiscible fluid components, which is

TABLE I. The study of mesh independence.

Number of mesh	3.3×10^7	4.5×10^7	6.3×10^7
Average of drag	56.6 N	55.8 N	55.8 N

suitable for tracking sharp interfaces. The segregated flow solver based on the SIMPLE algorithm is used to solve the velocity and pressure coupling problem, where the convection term adopts the mixed second-order upwind/bounded center scheme.

III. RESULTS AND DISCUSSION

A. Effect of structure on cavity development

1. Evolution of the cavity

The evolution of cavity can be divided into two stages: a stage of cavity development where the length of the cavity is increasing before 50 ms and a stage of cavity stabilization where the length of the cavity is basically unchanged after 50 ms. Figure 7 shows the development of cavity shape with an air volume fraction of 0.5. Compared to the condition without structure, the ventilated cavity with structure has a significantly different process of evolution and characteristics. At $t_0 + 10$ ms [Fig. 7(b)], the cavity develops steadily under the action of ventilation, but at this time, due to the presence of the structure, the shape of the cavity changes significantly, with more obvious compression at the upper edges of the cavity toward the side of the structure, such that the cavity shrinks and is squeezed toward the model. At $t_0 + 20$ ms [Fig. 7(c)], although the structure plays a certain role in hindering the evolution of the cavity, with the continuous increase in ventilation, the overall length and volume of the cavity gradually increase. Here, the length of the cavity exceeds the position of the structure, the compression of the structure on the cavity is weakened, and the volume of the cavity between the model and the structure increases. At the same time, the ventilated cavity is observed on the tail of the structure. It is worth noting that the effect of the structure leads to the shedding of small-scale vortices at the tail of the cavity, while there are no visible vortices shed without structure. Therefore, the existence of the structure increases the instability of cavity development. From $t_0 + 20$ ms [Fig. 7(c)] to $t_0 + 40$ ms [Fig. 7(e)], as the air continues to increase, the cavity gradually grows, and it begins to close deeply with the occurrence of deflation in the small-scale vortices in the tail. In addition, the presence of the structure accelerates deflation. At $t_0 + 30$ ms [Fig. 7(d)], parts of the vortices appear to shed in the case of a structure, but this feature appears at $t_0 + 40$ ms [Fig. 7(e)] without structure. Note that the overall length of the cavity without structure is longer than it is when the structure is present, as shown as red dotted lines. At the same time, the size of the ventilated cavity behind the structure gradually increases and envelops the structure. At $t_0 + 50$ ms [Fig. 7(f)], the cavity is basically stable, and the ventilated cavity no longer increases. The amount of air injected is approximately equal to the amount of air discharged from the tail, so the volume of the cavity is maintained at a constant value, and the cavity tends to be stable. In general, the presence of the structure causes the closed position of the cavity to advance, and the length of the stable section of the ventilated cavity is shortened. The deflation of the cavity is accompanied by the shedding of multi-scale vortices.

To analyze the mechanism of evolution of the ventilated cavity, streamlines and the volume fraction of water in the flow field at two typical times are extracted. The model is given as the absolute pressure at the current moment. Figure 8 illustrates the velocity streamline and the volume fraction of water at $t_0 + 20$ ms. Most of the area around the axisymmetric body, there is no cavity area and no large turbulence with a relatively regular flow field. However, in the tail region of the

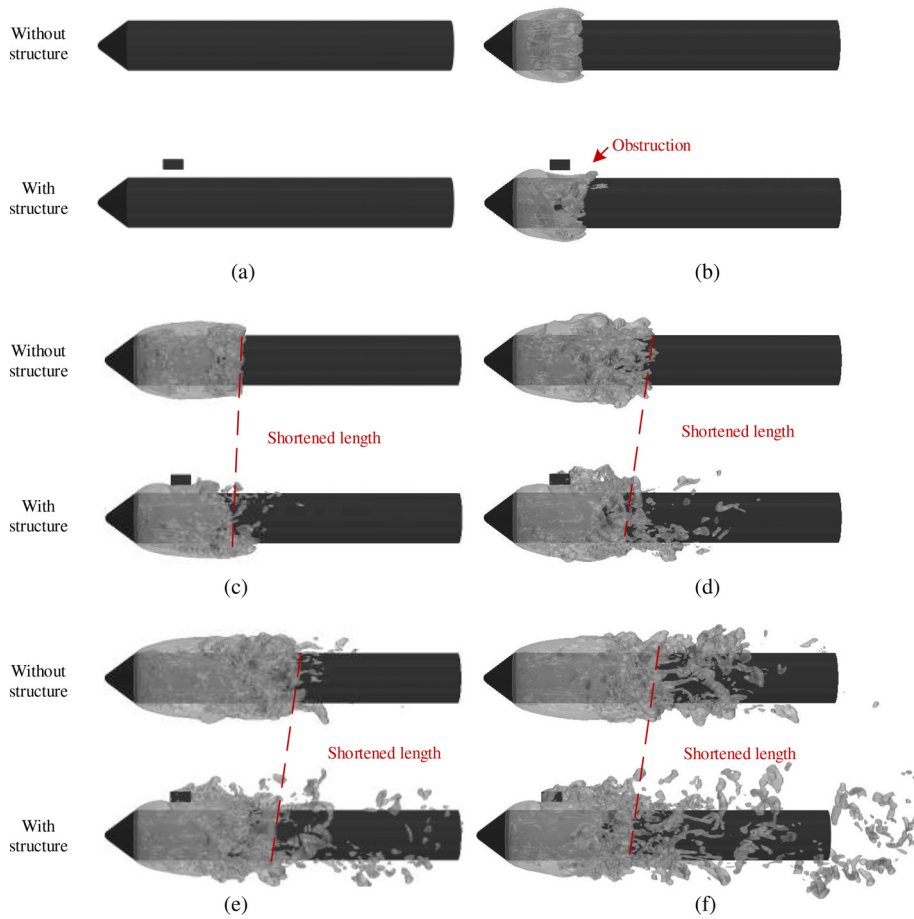


FIG. 7. The evolution of the cavity during the development stage (indicated by an air volume fraction of 0.5): (a) $t_0 + 0$ ms, (b) $t_0 + 10$ ms, (c) $t_0 + 20$ ms, (d) $t_0 + 30$ ms, (e) $t_0 + 40$ ms, and (f) $t_0 + 50$ ms.

axisymmetric body, the speed on both sides is higher than that of the tail, which can lead to the generation of a speed gradient and a re-entrant flow, and the upper and lower positions are symmetrically distributed [Fig. 8(a)]. Inside the cavity without structure, the ventilation port at the front of the model continuously delivers air to it. When the air at the front moves toward the back of the flow field, the speed gradually decreases. At the closed position of the tail, due to the effect of the re-entrant flow, a local high pressure is formed [Fig. 8(a)], and the volume fraction of water increases [Fig. 8(b)]. At this time, the tail air and the water are mixed with each other, which further reduces the speed, and a large number of vortices are formed inside the cavity. Under the action of the reversed pressure gradient, it moves to an area of low pressure at the front of the cavity. Hence, the turbulence generated inside the cavity makes the distribution of the velocity streamline irregular [Fig. 8(a)]. It is worth noting that the existence of the structure inhibits the development of the cavity. In front of the structure, the movement of the flow field is blocked, and there is a larger pressure fluctuation on the surface of the axisymmetric body. Simultaneously, because the cavity does not cover the area behind the structure, the velocity of the flow field in the gap between the structure and the model is faster, and this creates a velocity gradient. Therefore, in a certain area behind the structure, the streamlines are radial, and due to the influence of the structure, the cavity shows insufficient development, and

the local high pressure at the tail disappears. However, on the side without structure, the length of the cavity to the downstream is longer because of less obstruction of structure, and the same re-entrant flow appears as in the condition without structure.

Figure 9 illustrates the velocity streamline and the volume fraction of water at $t_0 + 40$ ms. The cavity continues to grow with the passage of time, and correspondingly, the low-pressure region on the surface of the model is further expanded. The gas-liquid mixing area in the cavity becomes longer, and the effects of turbulence are more evident [Fig. 9(a)]. In the downstream region of the cavity, the mixture of air and water is clearer, mainly because the volume fraction of water has increased [Fig. 9(b)]. It can also be seen that there are small-scale vortices shed from the end of the cavity. The structure inhibits the development of the cavity, but with the continuous inflow of air, the cavity gradually covers the surface of the structure. Therefore, the volume fraction of water around the structure decreases, and the vortices shedding occurs behind the structure are larger than the condition without structure.

2. Characteristics of vortex structures

Figure 10 shows the cross-sectional of the two-dimensional vorticity at two typical moments. This paper uses the third-generation

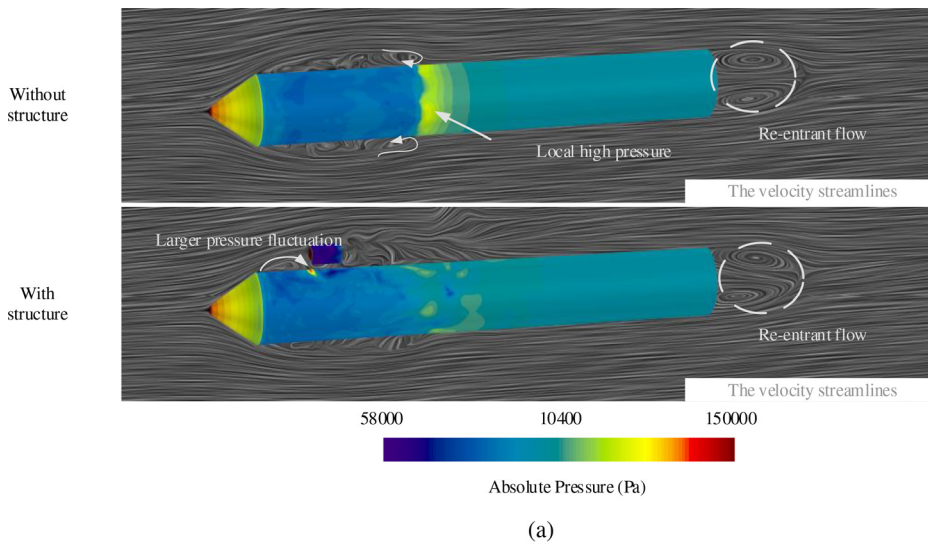
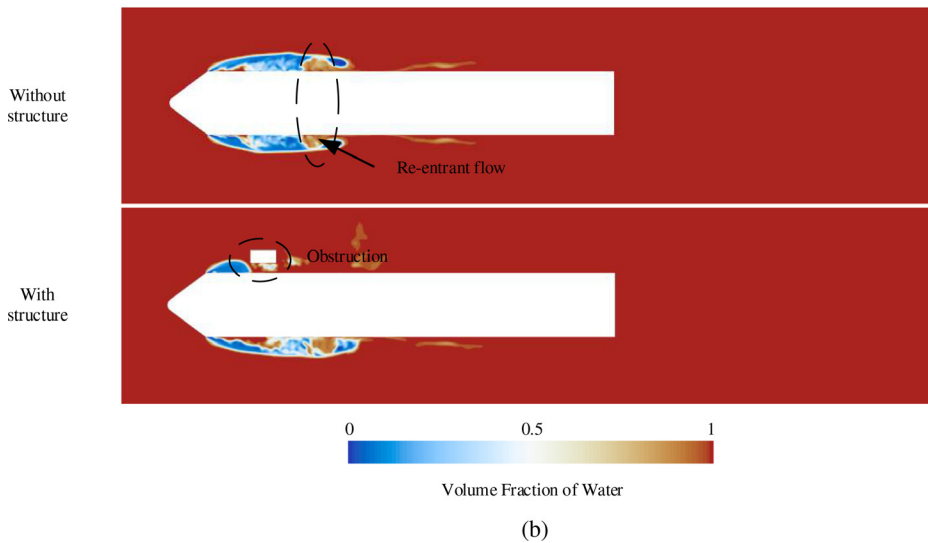


FIG. 8. At $t_0 + 20$ ms, the velocity streamlines, the pressure distribution, and the volume fraction of water near the axisymmetric body: (a) the velocity streamlines and the pressure distribution near the axisymmetric body and (b) the volume fraction of water near the axisymmetric body.



vortex identification method to analyze the vortex structures of the flow field. The Ω method can capture both strong and weak vortices at the same time, and there is no need to significantly adjust the threshold. Generally, the use of the Ω method can adequately identify the vortex structure of the flow field, which overcomes the problem of threshold selection in the second-generation vortex identification method. Liu⁴⁵ decomposes vorticity into a vortical part and a non-vortical part. The velocity gradient tensor V can be rewritten as

$$\nabla V = A + B, \tag{10}$$

where $A = \frac{1}{2}(\nabla V + \nabla V^T)$ is symmetrical, and $B = \frac{1}{2}(\nabla V - \nabla V^T)$ is anti-symmetrical.

Therefore, the Ω method is proposed,

$$\Omega = \frac{\|B\|_F^2}{\|A\|_F^2 + \|B\|_F^2 + \varepsilon}, \tag{11}$$

where ε is a positive number to avoid the denominator being zero, and $\|A\|_F^2, \|B\|_F^2$ represent the Frobenius norm of matrices A, B . Please see Refs. 46 and 47 for details.

At $t_0 + 20$ ms [Fig. 10(a)], the value of Ω in the flow field is generally low, which means that the development of the cavity is not sufficient, and the vortex motion characteristics are not obvious. However, the value of Ω inside the cavity is larger than that in the outer area, indicating a certain rigid rotational movement inside the cavity at this time. At the tail region of the model, there is a symmetrically distributed vortex structure due to the re-entrant flow caused by the difference in velocity gradient. However, the existence of the structure changes the evolution process of the ventilated cavity. At this moment, it can be found that there is a higher Ω value, accompanied by the shedding of small-scale vortices, which is visually distinct from the condition without structure. At $t_0 + 40$ ms [Fig. 10(b)], with an increase in ventilation time and the amount of air, the Ω value in the overall flow field area increases, and vortex motion in the flow field

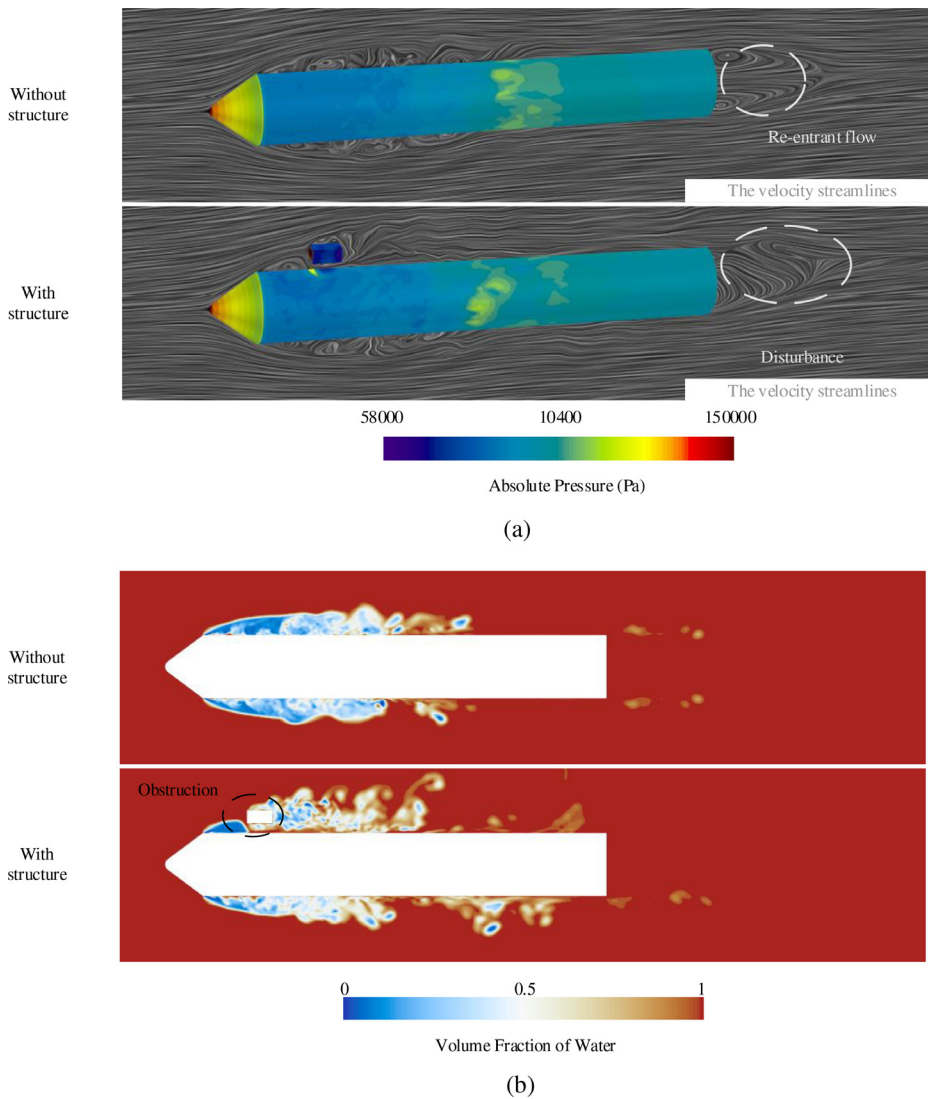


FIG. 9. At $t_0 + 40$ ms, the velocity streamlines, the pressure distribution, and the volume fraction of water near the axisymmetric body: (a) the velocity streamlines and the pressure distribution near the axisymmetric body and (b) the volume fraction of water near the axisymmetric body.

near the model gradually dominates. Due to the interaction between the air and water, the Ω inside the cavity is significantly higher than that at $t_0 + 20$ ms. At this moment, the characteristics of the vortex motion with or without structure show a significant difference. When there is no structure, the cavity develops in a relatively stable way, and there is no obvious closure or deflation. The overall vortex structures are small in scale, and the tail flow field area is still relatively symmetrical, but the value of Ω in the wake field increases, and the rotation effect is enhanced. The presence of the structure increases the size of the vortex structures where the cavity sheds, particularly in the flow field area at the end of the structure. Owing to the obstructive effect of the structure, the cavity in the front is not sufficient; it is squeezed in the narrow gap between the structure and the model and then diffuses behind the structure. Therefore, the area behind the structure shows a higher Ω value, and the shedding scale of the vortex structures is larger, with more intense shedding. At the same time, at the tail of the

model, the presence of the structure destroys the symmetry of the vortex structures of the flow field.

Figure 11 shows the view of the three-dimensional vorticity with an iso-surface of $\Omega = 0.52$ at two typical moments. (Coloring is done according to vorticity in the x direction $\zeta_x = \frac{\partial w}{\partial y} - \frac{\partial v}{\partial z}$, where v and w are the velocity components in the y and z directions, and the symbol of vorticity represents the direction of rotation.) At $t_0 + 20$ ms [Fig. 11(a)], as a result of the influence of the re-entrant flow from the tail, a larger vortex structure is produced at the tail of the axisymmetric body, but the vorticity value is 0 at this time; that is, there is no rotation effect in the x direction. However, on the surface of the cavity, a strong rotation characteristic appears. The existence of the structure increases the diameter of the cavity behind the structure and the size of the vortex structure at the tail. Near the structure, a large-scale vortex shedding phenomenon is clearly observed. At $t_0 + 40$ ms [Fig. 11(b)], as the ventilation time increases, the area covered by the

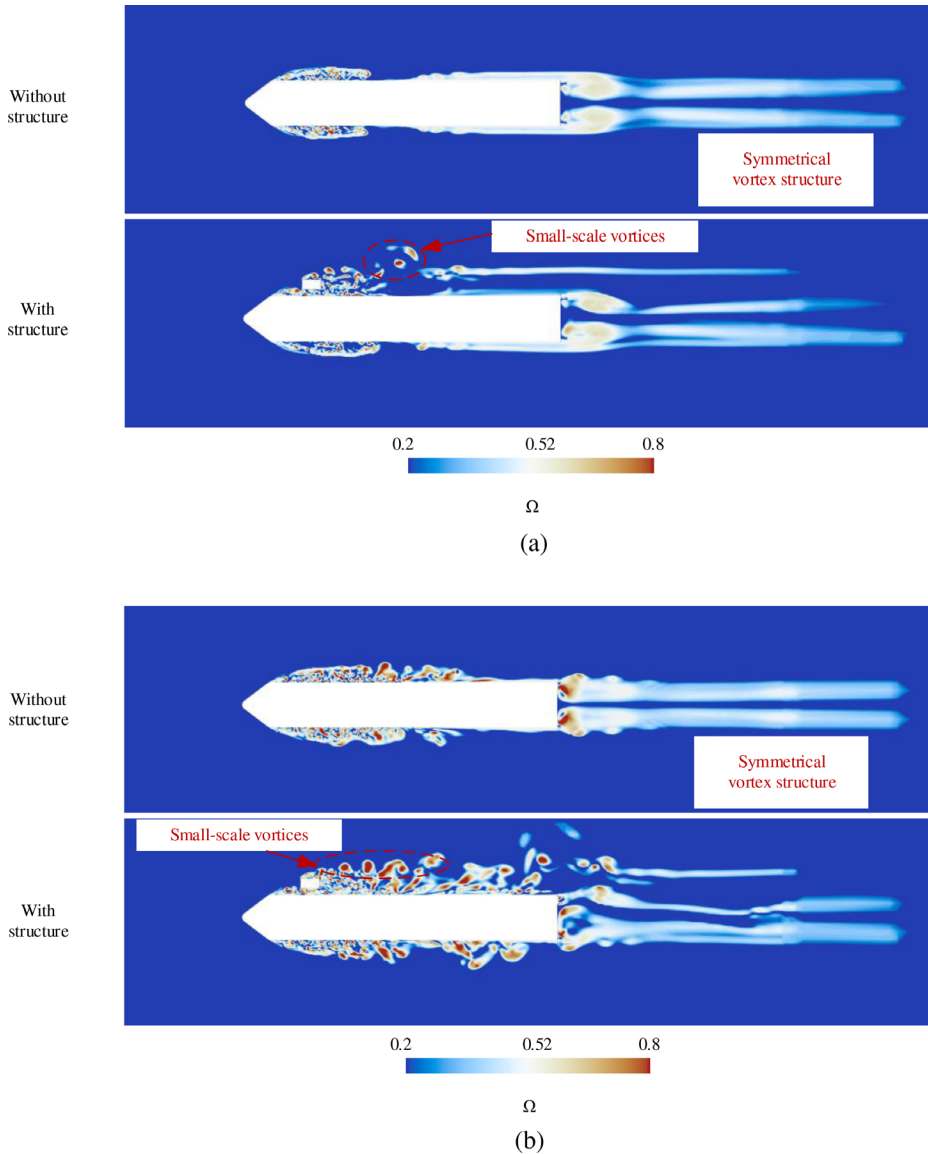


FIG. 10. Two-dimensional vorticity diagram at the development stage: (a) $t_0 + 20$ ms and (b) $t_0 + 40$ ms.

vortex structures increases. When there is no structure, the tail cavity begins to close and deflate, and the linear vortex structure at the closed position moves downstream along the wall of the axisymmetric body. However, in the condition with structure, the vortex structures at the tail of the model are shed more violently, and a large number of horseshoe-shaped vortices are generated, which basically cover the middle and rear sections of the entire model. The presence of structure accelerates the deflation of the tail and increases the scale of the vortices.

3. Cavitation number distribution inside cavity

The change in the ventilated cavitation number inside the cavity can reflect the evolution characteristics of the internal area of the cavity, which is helpful to analyze the internal relationship between the

development and shedding of the cavity. The flow of a ventilated cavity is generally described using the following formula:⁴⁸

$$\sigma_c = \frac{p_\infty - p_c}{\frac{1}{2} \rho_\infty V_\infty^2}, \tag{12}$$

where σ_c is the ventilated cavitation number, p_∞ is the pressure at infinity, p_c is the cavity pressure, and V_∞ is the mainstream velocity. We extracted the volume of the cavity and monitored the pressure values inside the cavity, using Eq. (12) to obtain the probability density of the ventilated cavitation numbers inside the cavity. Figure 12 provides the probability density of the ventilated cavitation number distribution in the cavity during the development stage. The peak 1 area is mainly distributed inside the ventilated cavity, with a larger ventilated cavitation number and lower pressure. The region of peak 2 is located at the

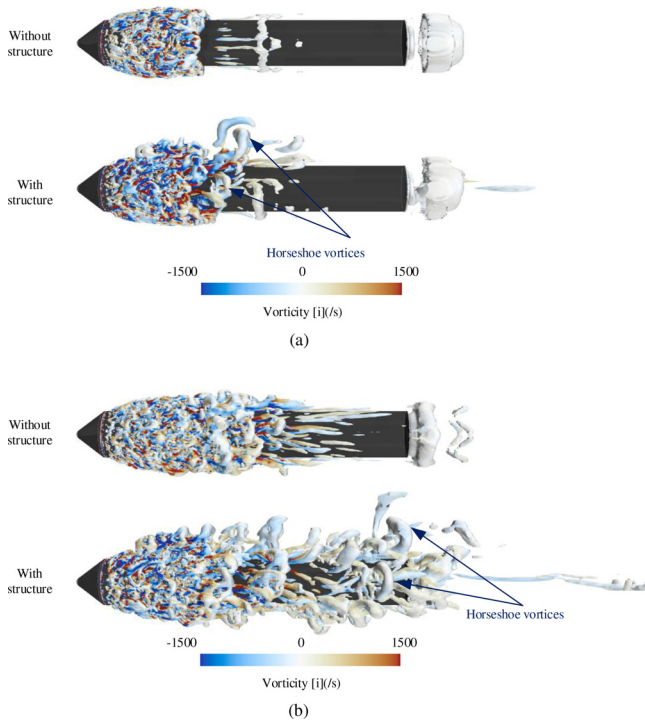


FIG. 11. Three-dimensional vorticity diagram: (a) $t_0 + 20$ ms and (b) $t_0 + 40$ ms.

closed position of the cavity, with a smaller ventilated cavitation number and higher pressure, but the probability value is small, and the phenomenon of cavity shedding is not obvious. In the interval between 0 and 0.16, the ventilated cavitation number in peak 2 under the condition with structure is smaller, and the probability increases. That is to say, at the closed position of the cavity, in the condition with structure, the pressure fluctuation is higher. In the two working conditions, peak 1 occupies most of the ventilated cavity, and the ventilated

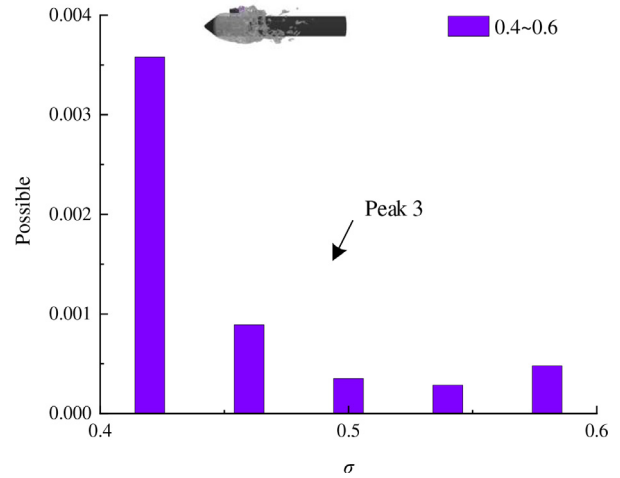


FIG. 13. Probability density of ventilated cavitation number distribution in the cavity in peak 3.

cavitation number inside the cavity changes gently. In the area with a larger ventilated cavitation number, the diameter of the cavity is also larger, and the diameter of the cavity decreases with the decrease in the ventilated cavitation number. Moreover, due to the existence of the structure, the ventilated cavitation number increases, and the area of peak 3 with a ventilated cavitation number ranging from 0.4 to 0.6 is distributed near the structure, although the probability value of the overall ventilated cavitation number is relatively small. The cavitation numbers inside the cavity are 0.26 and 0.27 with and without structure, respectively. In general, the presence of structure increases the pressure fluctuation of cavity shedding.

Figure 13 illustrates the probability density of ventilated cavitation number distribution in the cavity in peak 3 area. The ventilated cavitation number of area peak 3 is mainly concentrated in the range of 0.4–0.44, the probability tends to shrink and decrease, and the probability of the peak 3 area accounts for a small value of the ventilated

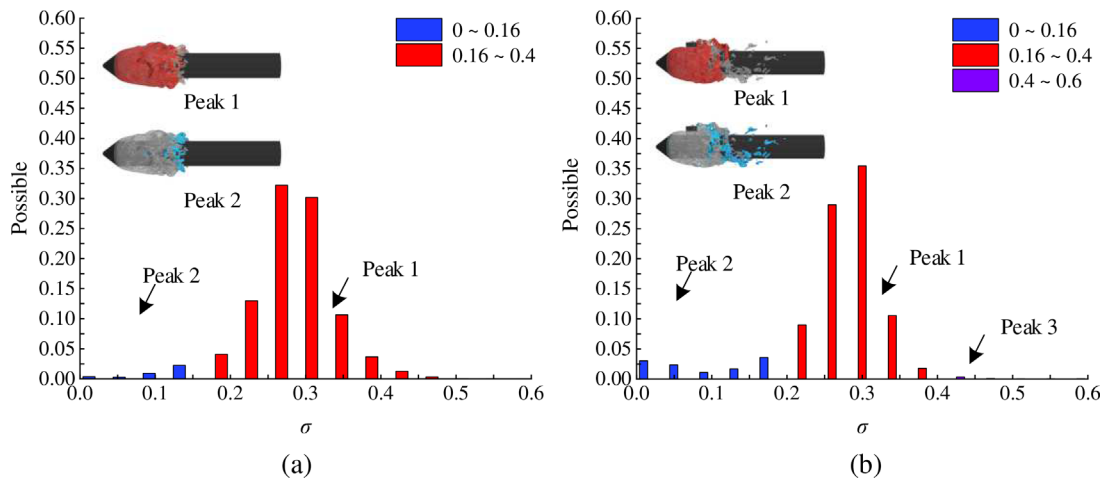


FIG. 12. Probability density of ventilated cavitation number distribution in the cavity during the development stage: without structure (a) and with structure (b).

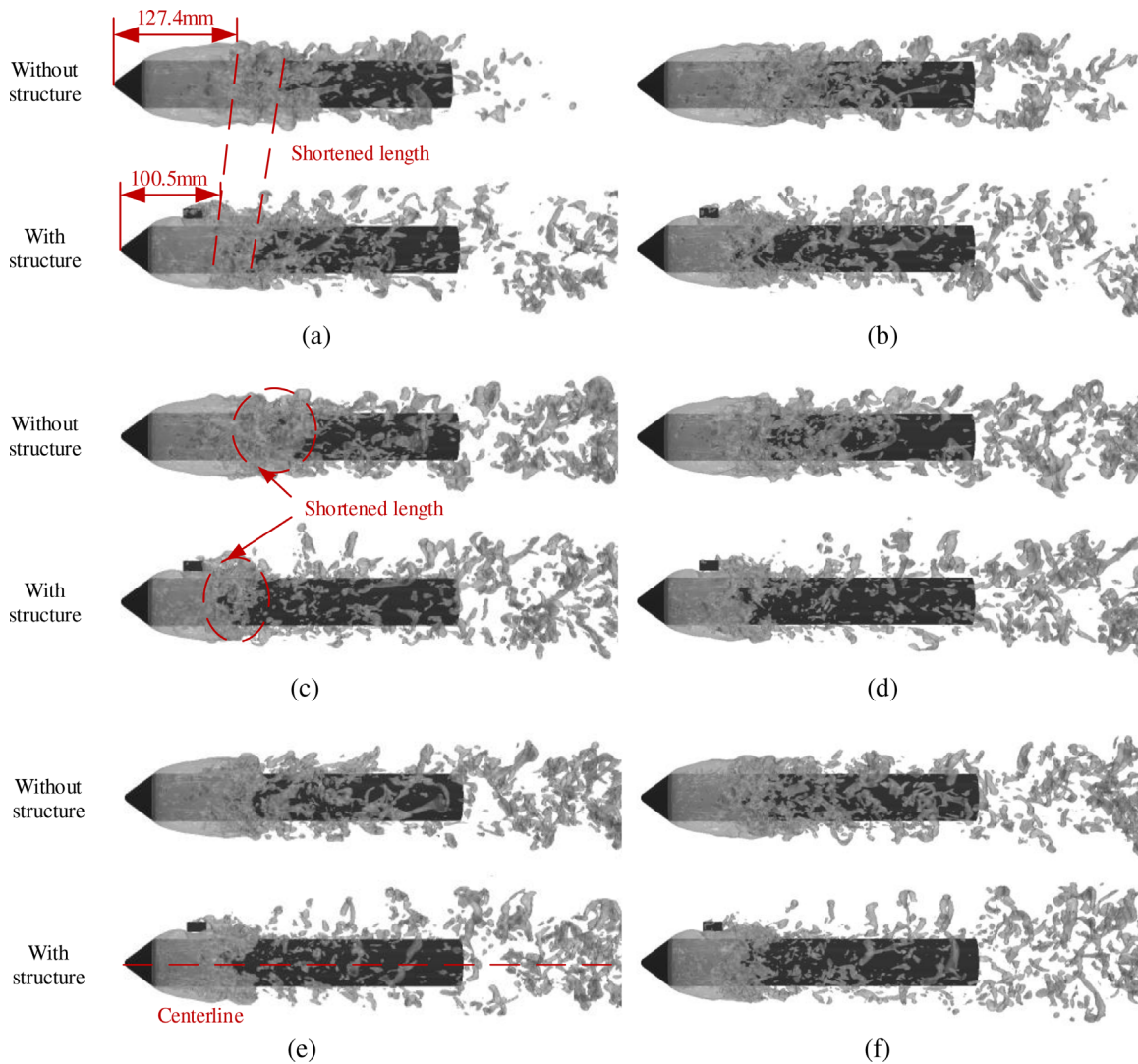


FIG. 14. Evolution of the cavity during the stable stage (indicated by an air volume fraction of 0.5): (a) $t_0 + 60$ ms, (b) $t_0 + 70$ ms, (c) $t_0 + 80$ ms, (d) $t_0 + 90$ ms, (e) $t_0 + 100$ ms, and (f) $t_0 + 110$ ms.

cavitation number. There is a higher pressure fluctuation, which leads to a strong disturbance in the wake region of the structure and larger-scale vortices shedding. However, in the condition without structure, the distribution of the high ventilated cavitation number in the peak 3 region is not generated. The presence of structure increases the instability of the flow field inside the cavity and increases the value of the ventilated cavitation number near the structure.

B. Effects of structure on cavity stabilization stage

1. Evolution of the cavity

When the cavity develops to the stable stage, the evolution of the cavity presents a periodic cycle. The shape of the cavity in one cycle is shown in Fig. 14. After $t_0 + 60$ ms, the cavity enters a stable stage, and

its length no longer increases. The length of the transparent cavity segment is measured as the main length of the cavity. The main lengths of the cavity in the two working conditions are 127.4 and 100.5 mm, respectively, and the presence of the structure resulted in a 21.1% reduction in the cavity length. On the whole, the overall evolution process and characteristic change in ventilated cavity under the condition with structure are basically the same as those under the condition without structure. From $t_0 + 60$ ms [Fig. 14(a)] to $t_0 + 100$ ms [Fig. 14(e)], the amount of air introduced and the air discharged is in dynamic equilibrium, so its length no longer changes significantly, but the presence of the structure causes the air release time to advance, beginning before $t_0 + 60$ ms. Therefore, the development of ventilated cavity is not as full as that under the condition without structure, and the length of the ventilated cavity is less than that of the condition

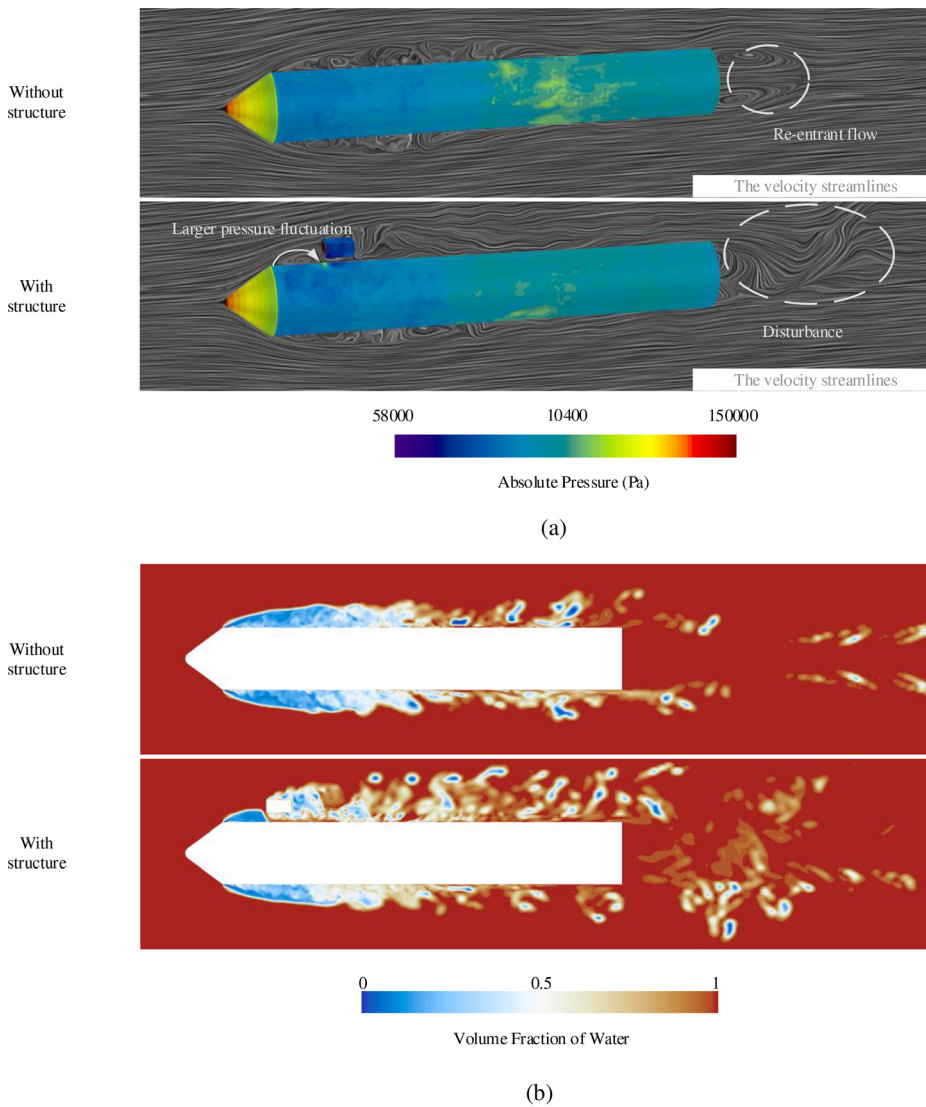


FIG. 15. At $t_0 + 60$ ms, the velocity streamlines, the pressure distribution, and the volume fraction of water near the axisymmetric body: (a) the velocity streamlines and the pressure distribution near the axisymmetric body and (b) the volume fraction of water near the axisymmetric body.

without structure, as shown by the red dotted line [Fig. 14(c)]. However, the overall size of the ventilated cavity is shortened under the action of structure, and the unstable section of air and water mixing is also shortened. Most notably, the existence of the structure changes the overall shape of the cavity in the stable stage above the model. At the front of the structure, the cavity shrinks to the inner wall of the model due to the obstruction of the structure, and the diameter is smaller than that in the condition without structure. When the cavity grows over the structure, the hindering effect of the structure disappears, the diameter of the cavity increases again, and a significant cavity cluster is attached to the wall behind the structure, which leads to asymmetry in the cavity. Similarly, the presence of the structure increases the shedding scale of the vortex structures, and due to the interference of the structure, the scale of the shedding cavity is also asymmetrical.

Figure 15 presents the streamlined velocity distribution and volume fraction of water at $t_0 + 60$ ms. At this moment, the ventilated

cavity reaches a stable state, and the length of the main body cavity will not increase with the increase in the ventilation time, and as the cavity grows, the air content gradually decreases. In the area covered by the cavity, the streamlined velocity presents the shape of the vortex due to the influence of the re-entrant flow, and the rotation effect of the velocity streamline in the latter part of the cavity is more obvious. The existence of the structure changes the evolution of the flow field inside the cavity above the model. At the front of the structure, the streamline in the stage of stability is largely consistent with that in the development stage. Due to the obstruction of the structure, a local flow will be produced and a high-pressure fluctuation will be generated on the surface of the model. However, at the trailing edge of the structure, with a large amount of air continuously ventilating inside the cavity and covering the flow field of the structure, the velocity streamlines behind the structure present a clear radial shape and move closer to the model wall in the process of backward transmission. The trend at this stage is significantly stronger than that in the development stage

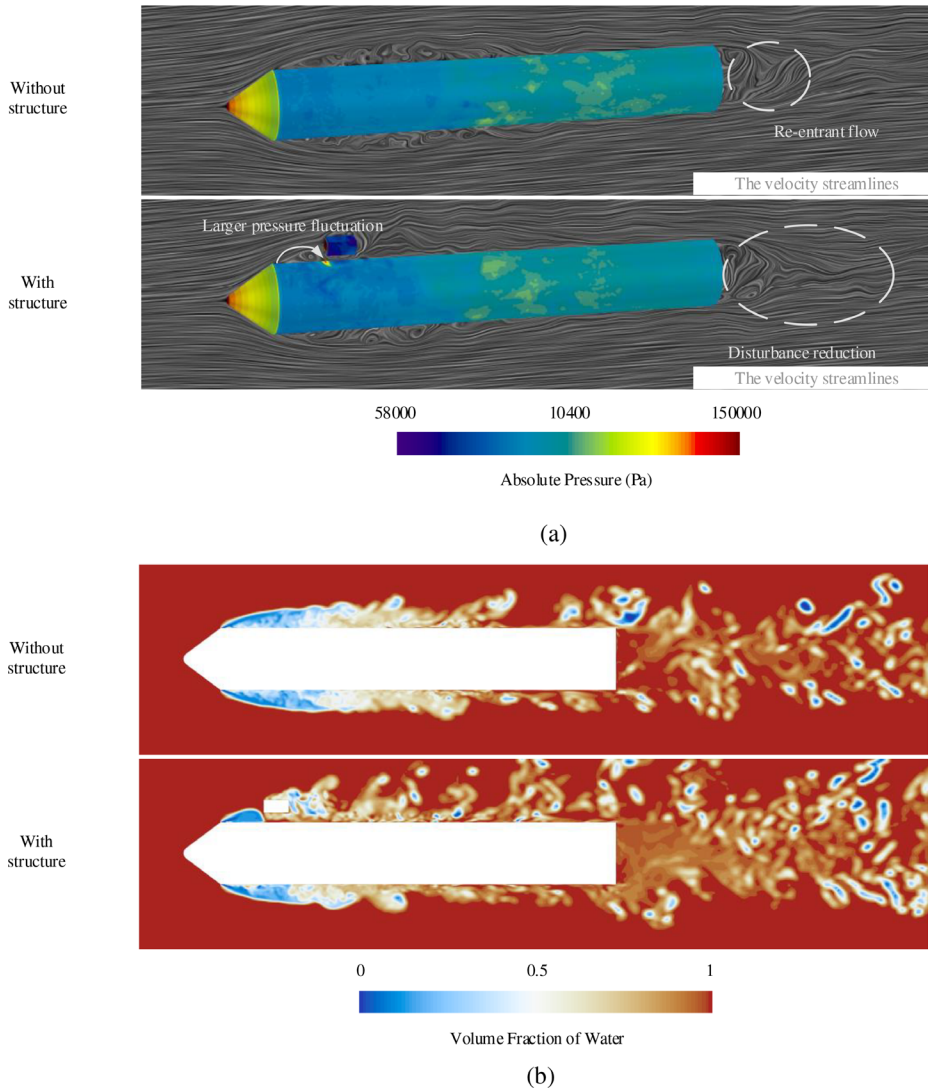


FIG. 16. At $t_0 + 100$ ms, the velocity streamlines, the pressure distribution, and the volume fraction of water near the axisymmetric body: (a) the velocity streamlines and the pressure distribution near the axisymmetric body and (b) the volume fraction of water near the axisymmetric body.

of the cavity. However, the flow field further affects the tail area of the model, causing a larger disturbance in the tail flow field where structure exists, as shown by the white curve [Fig. 15(a)]. At this time, the tail deflation method mainly refers to the way that the cavity sheds and the gas are entrained, indicating that there is no local high pressure similar to $t_0 + 20$ ms at the closed position behind the structure.

Figure 16 shows the velocity streamline distribution and the volume fraction of water at $t_0 + 100$ ms. At this stage, the cavity is nearly stable, and there is little difference between the whole streamline distribution from that at $t_0 + 20$ ms [Fig. 16(a)]. The inside of the cavity presents a larger velocity curl, but this is different from $t_0 + 20$ ms; at this moment, the disturbance area in the tail region becomes smaller [Fig. 16(a)], and the large-scale vortex structures have moved away. It can be seen from the volume fraction of water that there are only small-scale vortex structures at the trailing edge of the model at this time [Fig. 16(b)], and their main component is water, so the velocity

fluctuation is small, and the streamline disturbance in the tail is correspondingly reduced.

2. Characteristics of vortex structures

Figure 17 shows the cross section of two-dimensional vorticity in one cycle. At the stable stage of the cavity, the symmetrical vortex structure becomes small-scale vortices, and the Ω value increases due to the influence of the shedding of the cavity. From $t_0 + 60$ ms [Fig. 17(a)] to $t_0 + 100$ ms [Fig. 17(e)], with the continuous passage of air, the vortex structures in the flow field area increase, and the rigid vortex movement gradually takes the dominant position. The higher values of Ω all exist in the inside of the cavity. As the cavity of the tail closes and sheds, the size of the vortices increases, and the value of Ω increases. The presence of the structure increases the shedding size of the vortex structures on the side of the model near the structure.

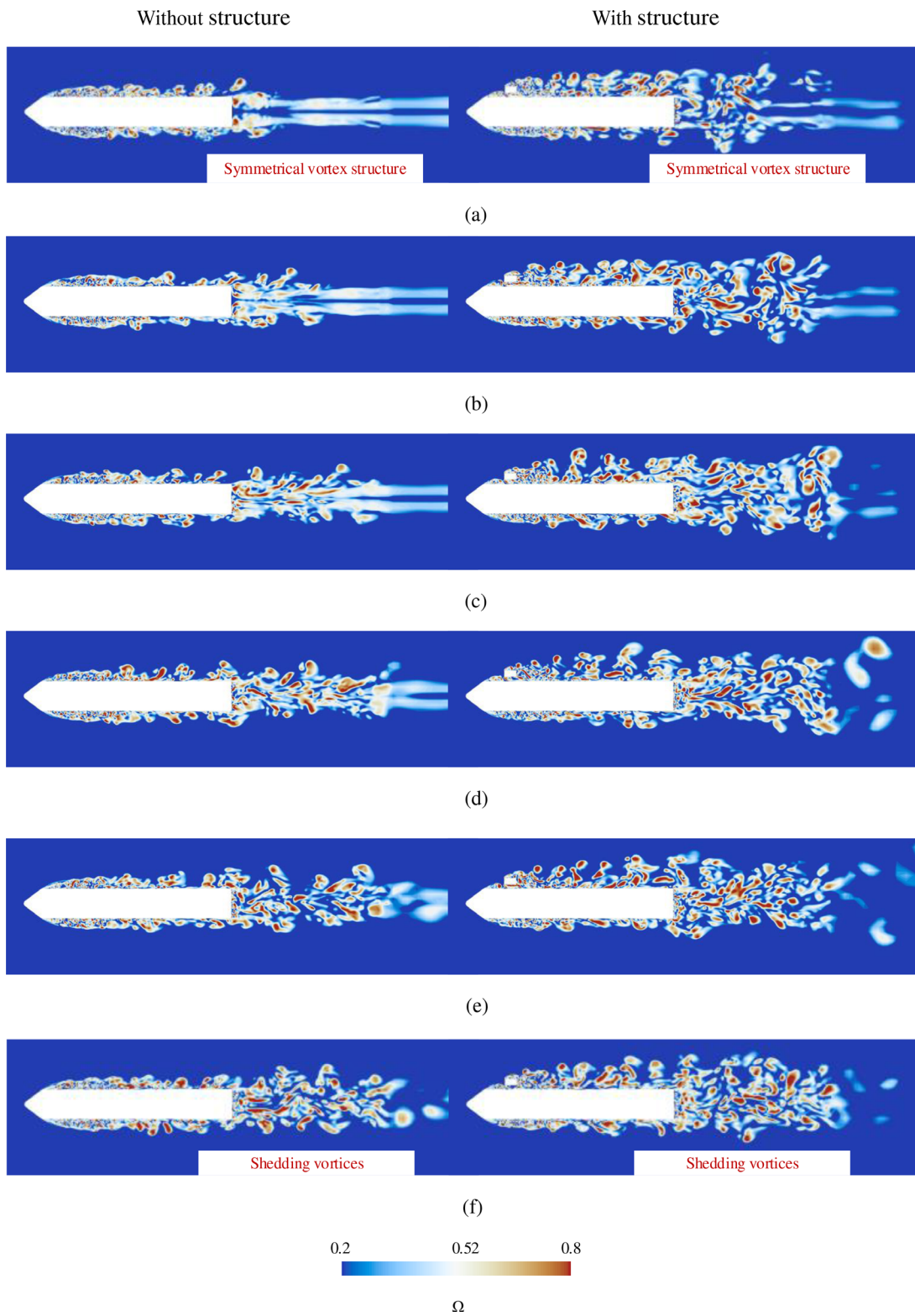


FIG. 17. Two-dimensional vorticity diagram at the stable stage: (a) $t_0 + 60$ ms, (b) $t_0 + 70$ ms, (c) $t_0 + 80$ ms, (d) $t_0 + 90$ ms, (e) $t_0 + 100$ ms, and (f) $t_0 + 110$ ms.

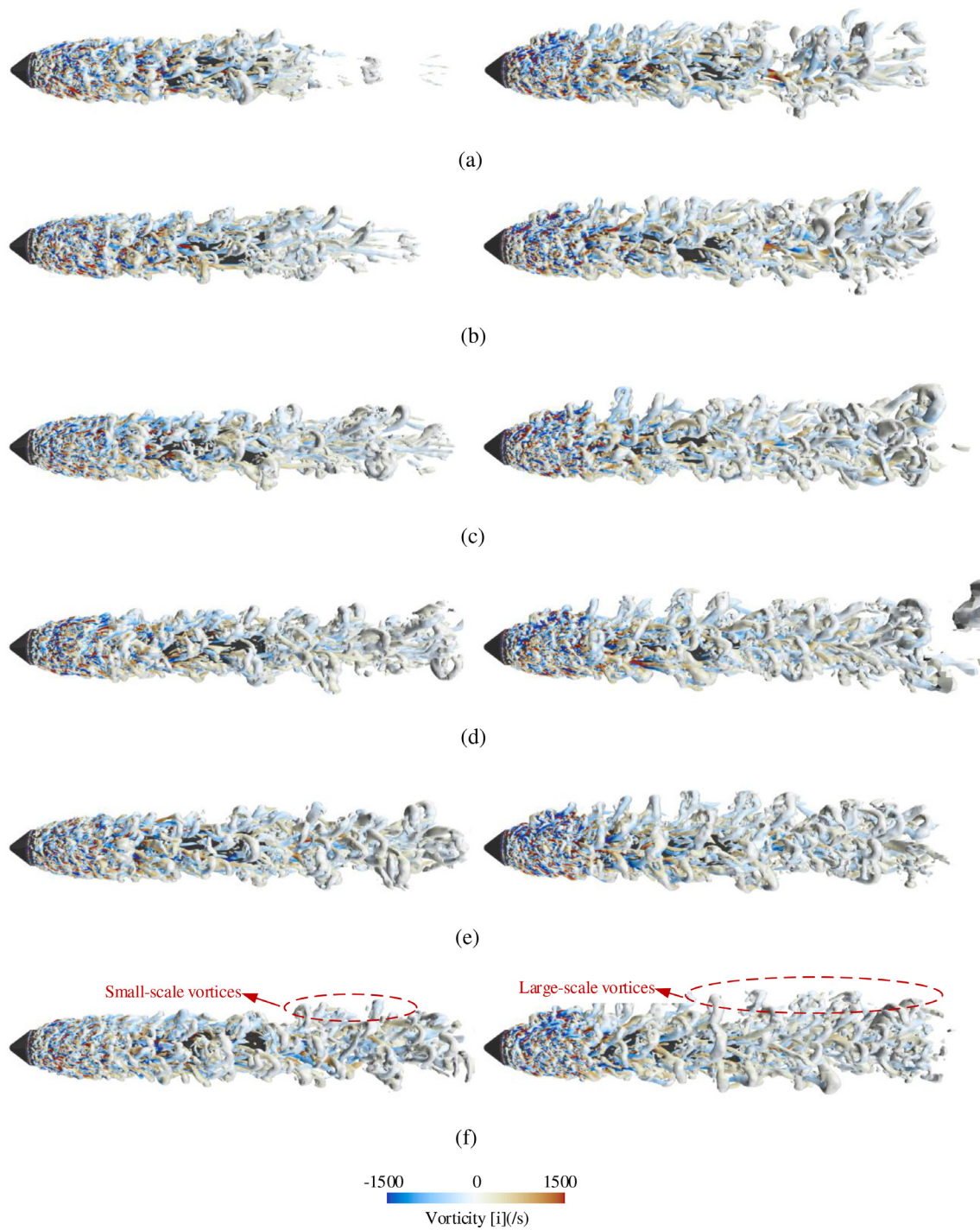


FIG. 18. Three-dimensional vorticity diagram at the stable stage: (a) $t_0 + 60$ ms, (b) $t_0 + 70$ ms, (c) $t_0 + 80$ ms, (d) $t_0 + 90$ ms, (e) $t_0 + 100$ ms, and (f) $t_0 + 110$ ms.

The ventilated cavity at this stage basically envelops the structure, which increases Ω of the flow field near the structure and produces a strong turbulence effect on the rear. Therefore, the shedding scale of the vortices is larger, and the shedding is more intense.

Figure 18 shows a view of the three-dimensional vorticity with an iso-surface of $\Omega = 0.52$ in one cycle. At $t_0 + 60$ ms [Fig. 18(a)], when there is no structure, the ventilated cavity enters a stable stage, and the vortex structures are not fully developed. Therefore, in the wake of the

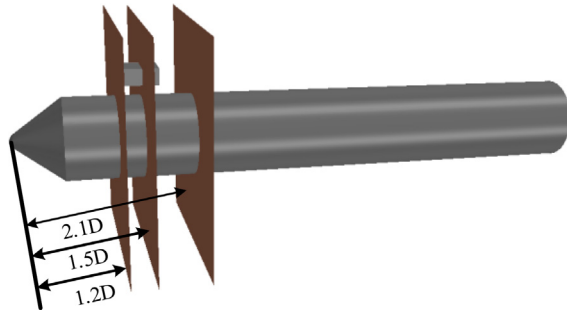


FIG. 19. Distribution of mid-section in vorticity.

model, the vortex structures of the structure condition are stronger than those of the condition without structure. From $t_0 + 70$ ms [Fig. 18(b)] to $t_0 + 100$ ms [Fig. 18(e)], the large-scale vortices continue to shed and cover the entire wake field. In other words, the existence of the structure increases the scale of the vortex shedding. At the tail of the structure, the attached ventilated cavity sheds, which leads to vortices of a certain scale in the flow field behind the structure. With the incoming flow, the vortices interact with the vortices from the main body, which further increases the scale of the vortices. At $t_0 + 110$ ms [Fig. 18(f)], a new cycle begins. Under the condition without structure, the vortices also fill the entire wake field.

To provide a representation of the vortex structures where the cavity is stable, Fig. 20 shows the cross section of vortex structures at three locations in the flow field at two typical moments. Among them, the position of the mid-section in the basin is shown in Fig. 19. The distance between the three cross sections and the head of the axisymmetric body are $1.2D$, $1.5D$, $2.1D$, respectively. At $t_0 + 60$ ms, the wall of the model shows a larger vorticity absolute value in the presence of the structure at $1.2D$. In this process, the development of the front cavity is hindered by the structure, and a mixture of air and water moves along the surface of the model toward the shoulder, creating larger vortices. Consequently, in the presence of the structure, the

positive and negative values of vorticity on the surface of the wall are larger, as shown by the dotted line in Fig. 20. At $1.5D$, the presence of the structure increases the velocity between the axisymmetric body and the structure, while the velocity behind it is small, thus forming a larger velocity gradient, which causes the absolute value of the vorticity here to be greater than it is when there is no structure. Furthermore, the vorticity around the structure is also higher due to the attachment of the cavity, as shown by the dotted line in Fig. 20. At the position of $2.1D$, the wake field behind the structure forms a large positive and negative vorticity region due to the shedding of cavities, the size of which is largely the same as the size of the structure, and around the model, the distribution of vorticity under the two working conditions is basically the same. At $t_0 + 100$ ms, the distribution of vorticity is almost the same as that at $t_0 + 60$ ms, that is to say, at the stable stage of the cavity, the evolution characteristics of the cavity basically remain unchanged, and the differences in vorticity distribution are small.

3. Cavitation number distribution inside cavity

Figure 21 shows the probability density of the ventilated cavitation number distribution in the stable stage. Similarly, in the stable stage of the cavity, the ventilated cavitation number in peak 1 is larger, and the internal pressure is lower, but the probability is reduced. The area of peak 2 is largely distributed in the closed position of the cavity tail and the shedding cavities, which produces a higher pressure fluctuation. At this stage, large-scale shedding vortices are generated at the tail of the cavity. Therefore, the probability distribution of peak 2 area increases, occupying the dominant position of pressure fluctuation. However, under the two working conditions, peak 1 area still occupies most of the ventilated cavity, and the ventilated cavitation number inside the cavity changes more slowly. In the peak 2 area and the closed position of the tail, the ventilated cavitation number fluctuates greatly, and the higher probability density is concentrated near the small, ventilated cavitation number. With or without structure, the cavitation numbers inside the cavity are both 0.12. The presence of the structure has little effect on the cavitation number, but changes the distribution density of the cavitation number.

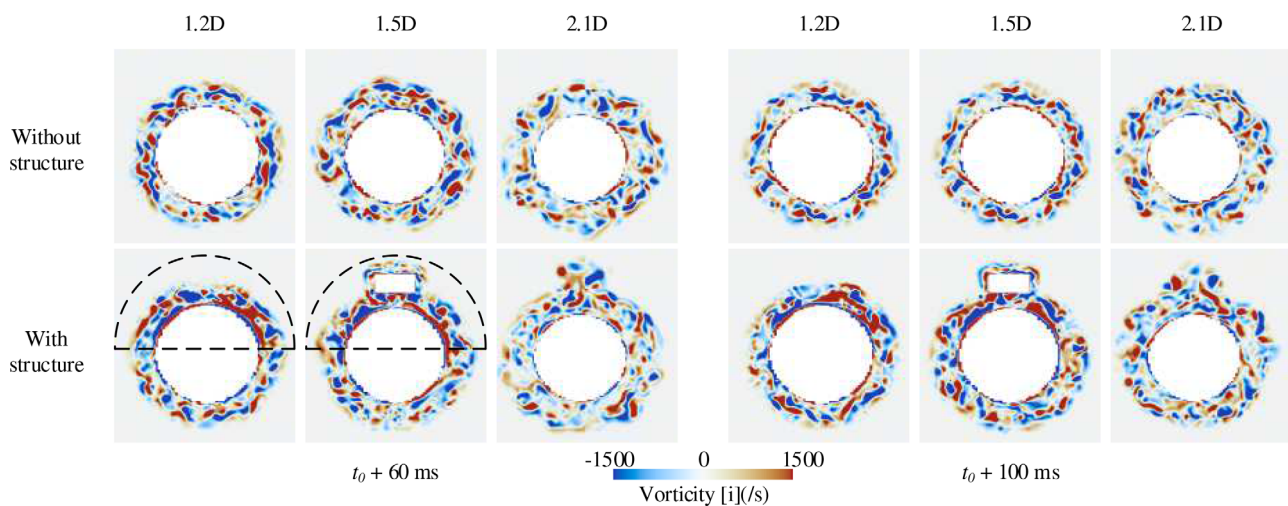


FIG. 20. Mid-section two-dimensional vortex structures.

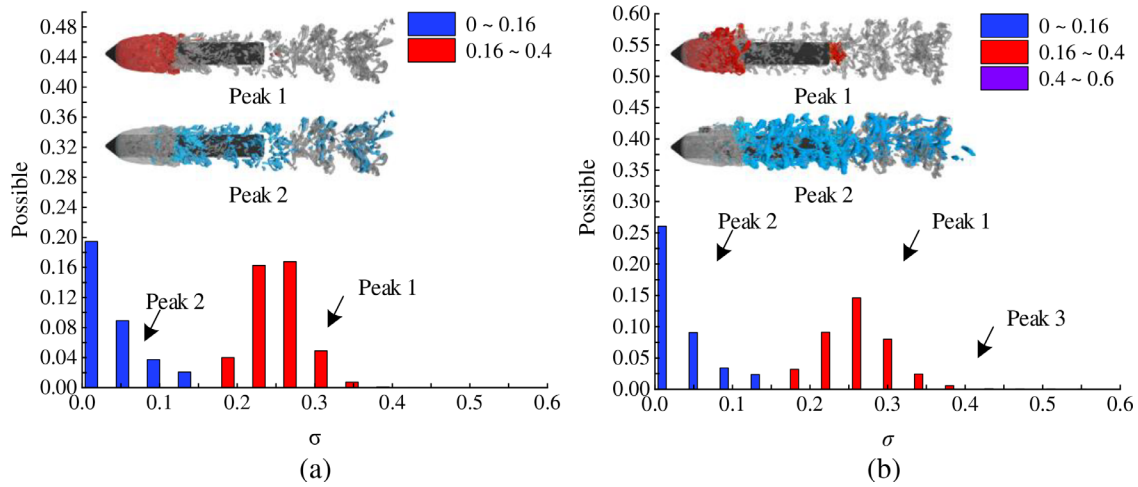


FIG. 21. Probability density of ventilated cavitation number distribution in the cavity during the stable stage: without structure (a) and with structure (b).

Figure 22 shows the probability density of the ventilated cavitation number distribution in the cavity in the peak 3 area. The observation shows that the main body cavitation number of peak 3 area is concentrated in the interval of 0.4–0.44, and the probability shows a decreasing trend. The probability of peak 3 area accounts for the smaller probability of the overall ventilated cavitation number. At this time, a certain pressure fluctuation occurs, which causes a local low pressure near the structure and then causes a strong disturbance in the structure wake region, resulting in large-scale vortex shedding. There is no high ventilated cavitation number distribution in the peak 3 area in the condition without structure. In general, the presence of the structure increases the instability of the flow field inside the cavity and increases the value of the high ventilated cavitation number, and the pressure distribution becomes more complex.

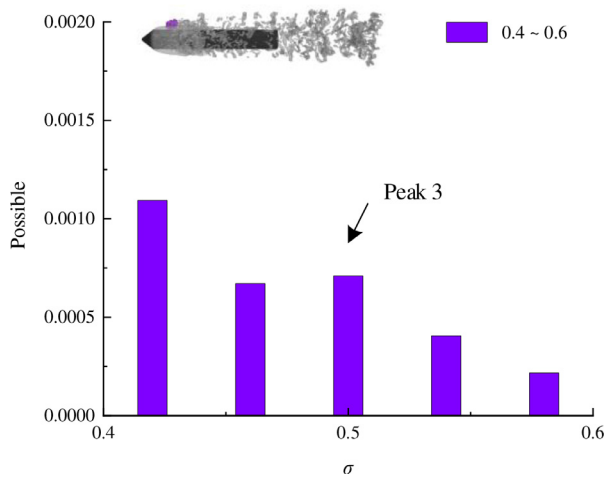


FIG. 22. Probability density of ventilated cavitation number distribution in the cavity in peak 3.

C. Load analysis of cavity evolution

1. Lift drag characteristics

Figure 23 shows the comparison of lift (a) and drag (b) with or without structure. The structure has little effect on the lift, but the lift fluctuation is obvious in the cavity development stage. After $t_0 + 50$ ms, the lift is stable gradually and changes periodically, and the lift with or without structure is basically the same, with an average of 7.44 and 6.04 N, respectively. However, there is a large difference in resistance characteristics. Particularly, in the cavity development stage, due to the growth of the cavity, the pressure in the condition without structure gradually decreases, while the resistance increases under the condition with structure. The presence of structure hinders the growth of the cavity, which makes the size of the cavity above the model smaller than the size of the cavity below. Due to the asymmetry of the cavity, the pressure drag of the model is large at the stage of cavity development and then produces a larger total resistance. When the cavity enters the stable stage, the resistance gradually stabilizes, and the total resistance reaches 53 and 55 N with or without structure, respectively. The existence of structure reduced the lift of the axisymmetric body by 18.9% and increased the resistance by 3.8%.

2. Pressure fluctuation characteristics of monitoring points

Figure 24 shows the comparison of the pressure fluctuation at the two pressure monitoring points P1 (a) and P2 (b) with or without structure. From $t_0 + 10$ ms to $t_0 + 50$ ms, the cavity is in the developing stage, and the pressure at the two monitoring points P1 and P2 gradually increases. After $t_0 + 50$ ms, the pressure value gradually stabilized to a certain range and showed periodic oscillation. It is noteworthy that in all cases, the pressure at the P1 monitoring point is almost the same with or without structure, and the average difference is 2.3%, but the pressure oscillation is more severe with structure. The difference between the peak and valley values of the pressure under the condition without structure is 11.3%, and that under the condition

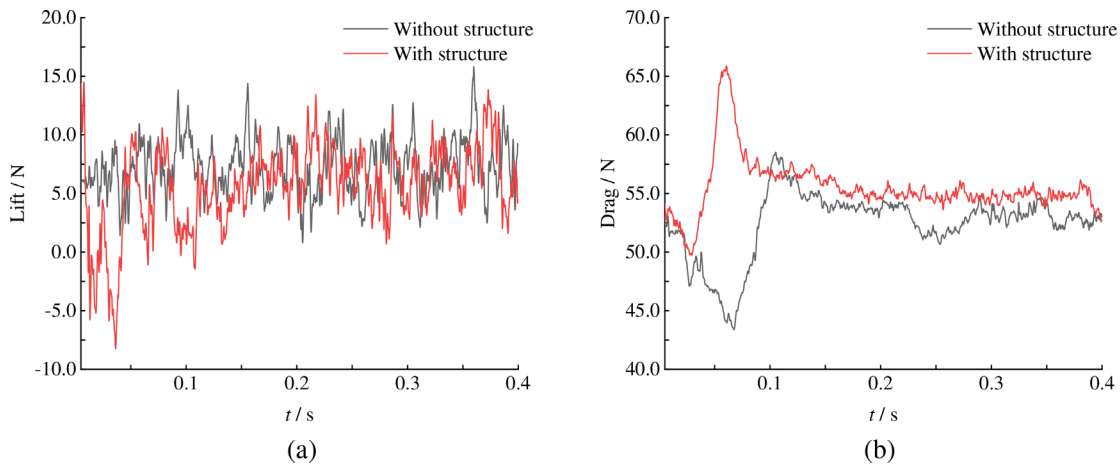


FIG. 23. Comparison of lift (a) and drag (b) with and without structure.

with structure is 17.4%. However, at point P2, the pressure fluctuation amplitude increases significantly with significant pressure fluctuations in the presence of structure. Under the condition without structure, the pressure fluctuation is basically stable, and the law is the same as that of the P1 monitoring point, with a difference of 9.4% between the peak and the valley values. Figure 25 is a schematic diagram of the surface pressure of the model at a certain moment, showing that part of the incoming flow moves along the structure to the model because of the blocking effect of structure, forming an impact re-entrant flow and a larger pressure pulse on the surface of the model. Therefore, the pressure fluctuation amplitude at the P2 pressure monitoring point is significantly increased, with a difference of 37.7% between the peak and the valley values. The presence of structure increased the average pressure by 25.7%.

Figure 26 shows the pressure fluctuation at the two pressure monitoring points P3 (a) and P4 (b) with and without structure. At P3, which is directly below the center of the structure, the value of the pressure is smaller than that under the condition without structure,

which is reduced by 16.2%. However, the presence of the structure increases the disturbance inside the cavity, and the pressure fluctuation is more violent. The difference between the peak and valley values of the pressure under the condition without structure is 9.8%, and that under the condition with structure is 57.6%. Between $t_0 + 10$ and $t_0 + 20$ ms, the pressure at P4 fluctuates greatly and decays rapidly. After $t_0 + 20$ ms, the pressure at P4 gradually stabilized at 9.0×10^4 Pa. There is a little difference between the two conditions at this pressure monitoring point, only a difference of 0.6%. However, because the vortex shedding scale is larger under the condition with structure, the pressure fluctuation amplitude captured by the monitoring point is larger. The difference between the peak and valley values of the pressure under the condition without structure is 9.0%, and that under the condition with structure is 20.9%. Figure 27 gives a schematic diagram of the surface pressure of the model at a certain moment, showing that one part of the incoming flow moves along the structure surface to the model because of the hindrance of structure, and the other part of the incoming flow moves backward along the gap between the structure

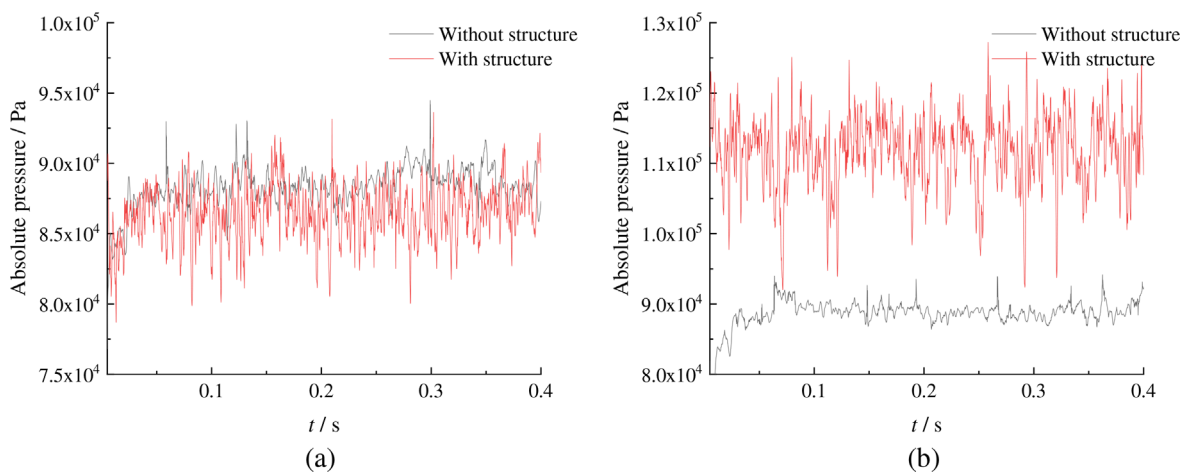


FIG. 24. Comparison of pressure fluctuations on the surface of the model at P1 (a) and P2 (b).

14 March 2024 07:44:42

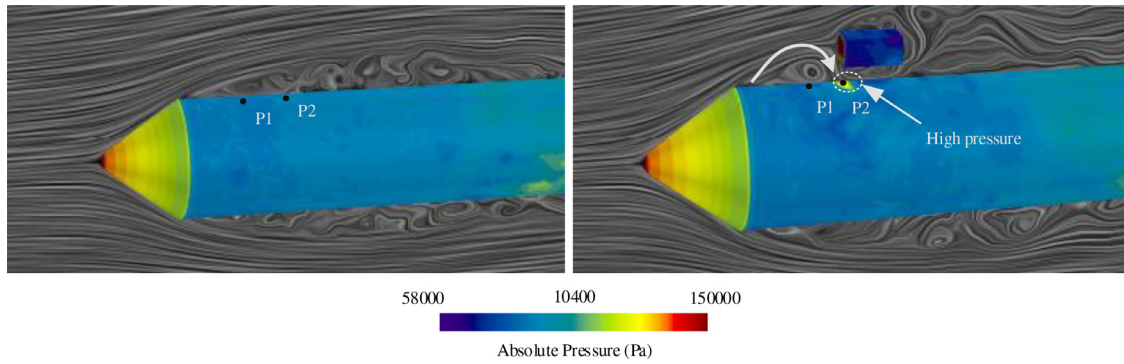


FIG. 25. Pressure and velocity streamline distribution on the surface of the model (P1 and P2 are shown in the figure).

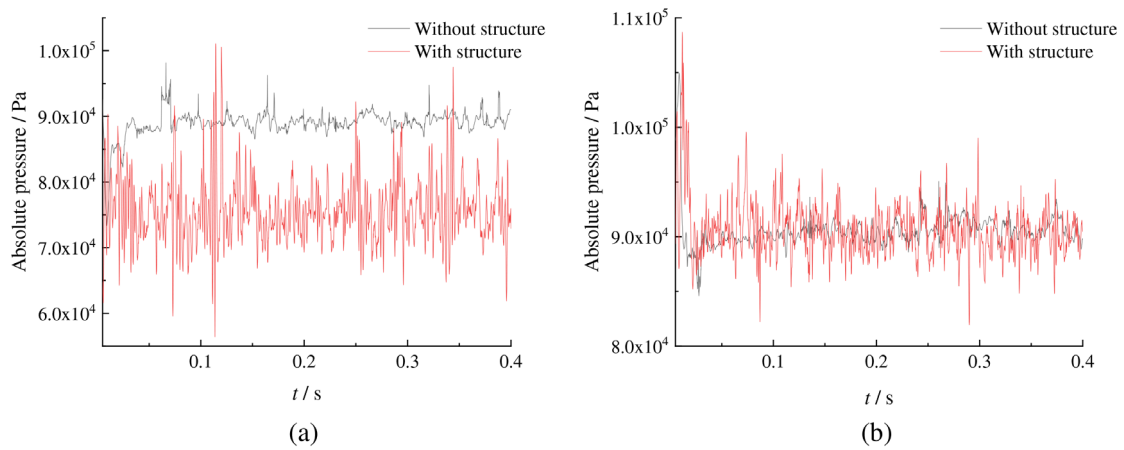


FIG. 26. Comparison of pressure fluctuations on the surface of the model at P3 (a) and P4 (b).

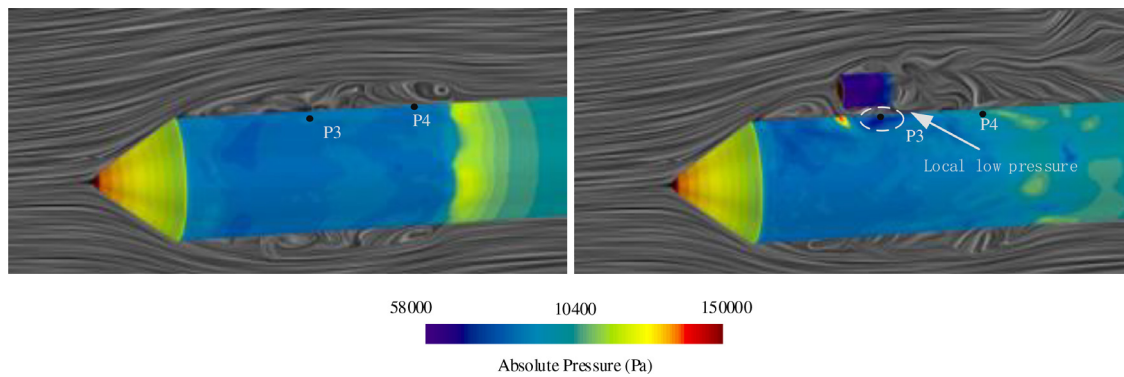


FIG. 27. Pressure and velocity streamline distribution on the surface of the model (P3 and P4 are shown in the figure).

and the model. The velocity of the flow field increases in this part, thereby forming a local low-pressure area directly below the structure center, which causes the pressure of the P3 monitoring point under the condition with structure to be smaller than that under the condition without structure.

We performed FFT on 5000 data using a rectangular window function, where the sampling frequency was 10 kHz, resulting in a frequency resolution of 2 Hz. Figure 28 shows the frequency distribution diagram of the power spectral density (PSD) of the pressure monitoring points P2 (a) and P3 (b) in the stable stage of the cavity.

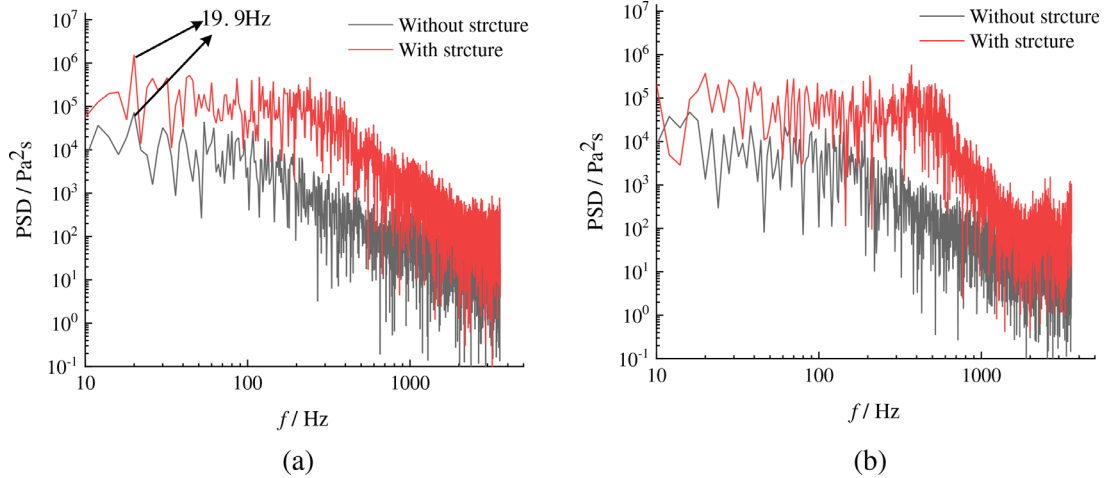


FIG. 28. Comparison of power spectral density (PSD) corresponding to pressure fluctuation at monitoring points P2 (a) and P3 (b).

The existence of the structure does not change the periodic characteristics of the ventilated cavity in the front of the structure. The main frequency of the ventilated cavity shedding is 19.9 Hz, and the period is 0.05 s under both conditions. However, in the condition without structure, as the ventilation speed slows, the frequency of ventilating cavity at P3 also decreases slightly, to 15.9 Hz, a decrease in 25%. The presence of the structure increases the pressure fluctuation at this point and advances the deflation of the cavity, thereby shortening the main dimension of the ventilating cavity, which makes it enter the stable stage earlier, and increasing the main shedding frequency of the ventilating cavity, which is consistent with the main shedding frequency at P2 in the front of the structure. It is worth noting that when the structure is present, the instability of the ventilation cavity increases, and the energy value of the shedding is also higher.

Figure 29 shows the comparison diagram of the first five-order frequencies at P2 (a) and P3 (b). The shedding frequencies of the first five orders of the ventilated cavity under the structure condition are slightly greater than those in the condition without structure, and with

the increase in the order, the difference between the two becomes more and more obvious. This is because a narrow tube effect appears between the structure and the vehicle, which increases the air velocity in that location, and the larger vorticity causes the ventilating cavity to shed more violently under the condition with structure.

3. Pressure fluctuation characteristics of detection lines

To better analyze the influence of structures on the surface pressure fluctuation, detection lines L1, L2, and L3 are established at three positions on the model wall, as shown in Fig. 30. Figure 31 shows the pressure curve of the model surface at $t_0 + 150$ ms. In the front of the model, the pressure in the area covered by the cavity is low and the fluctuation is gentle, but there is a high-pressure peak at the shoulder of the model for ventilation. At 0.2 m from the head, owing to the deflation and closure of the cavity, larger vortices are generated, which in turn cause the pressure to rise. During the downstream movement of the shedding cavity, there is a significant pressure fluctuation on the

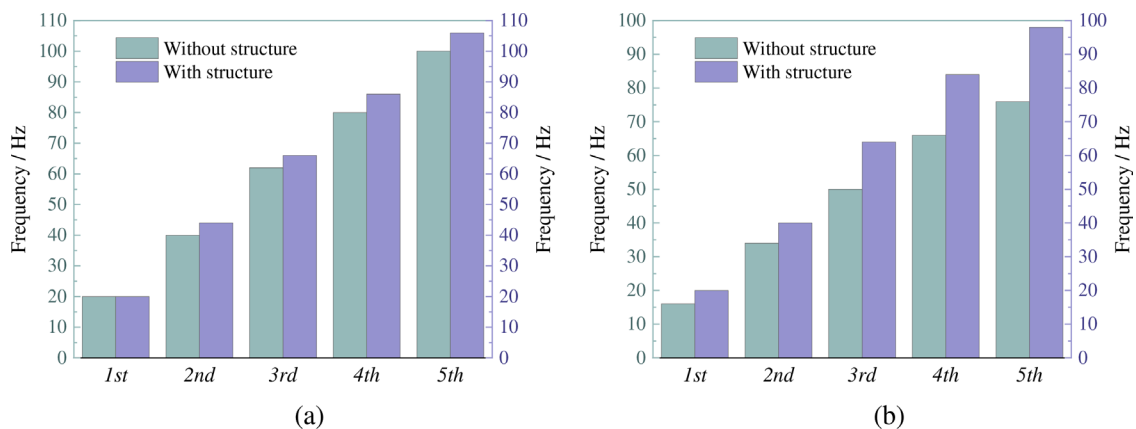


FIG. 29. Comparison of the first five-order frequencies of power spectral density (PSD) corresponding to pressure fluctuation at monitoring points P2 (a) and P3 (b).

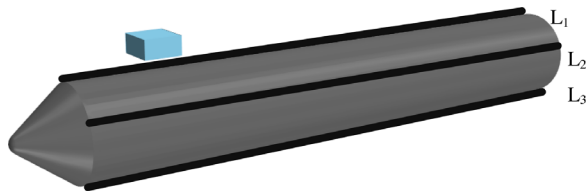


FIG. 30. Pressure detection lines on the surface of the model.

model wall. In addition, at detection line L1, the presence of the structure produces a large pressure fluctuation at 0.06 m. This is because of the obstructive effect of the structure, causing the flow to hit the surface of the model and generate local high pressure. At the position of 0.06–0.75 m, the increase in the flow velocity causes the pressure to drop rapidly, which is also the same as the previous conclusions.

IV. CONCLUSIONS

In this paper, a numerical simulation analysis of the evolutionary mechanism of a ventilated cavity flow field is carried out. The effects of the presence or absence of a structure on the evolution of cavity

shape, the velocity distribution of the flow field, the vortex structures, and the pressure fluctuation are compared in detail. The main conclusions are as follows:

- (1) During cavity development, the existence of the structure changes the flow characteristics inside the cavity. The presence of the structure shortens the length of the stable section of the main body of the ventilated cavity and advances the deflation. At the same time, the symmetry of the flow field in the wake field area of the model is destroyed, and the tail vortex structures shed more violently under icy conditions. But the cavitation number changes relatively smoothly.
- (2) In the stable stage of the cavity, the presence of the structure changes the overall shape of the cavity above the model, which makes it shrink to the sidewall of the model. As the cavity grows over the structure, its hindering effect disappears, and the diameter of the cavity increases again. At the same time, the presence of the structure increases the scale of vortex shedding. The structure leads to an increase in the probability distribution of lower ventilated cavitation number inside the cavity.
- (3) The presence of the structure affects the lift-drag characteristics around the model. It also makes the fluctuation of the model

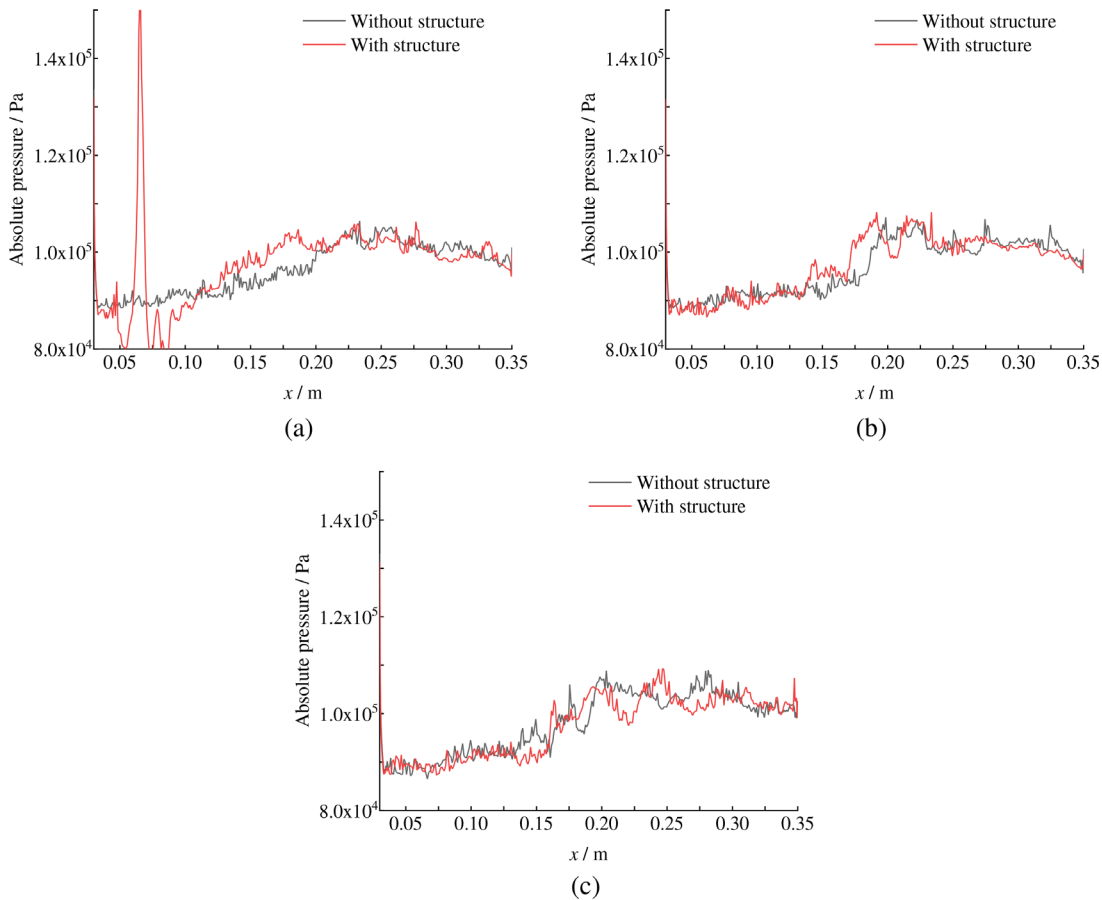


FIG. 31. Pressure detection lines [L1 (a), L2 (b), and L3 (c)] on the surface of the model: (a) pressure fluctuation at L1, (b) pressure fluctuation at L2, and (c) pressure fluctuation at L3.

pressure more violent, and the characteristics of pressure fluctuation vary by region. The pressure in the area between the model and the structure is reduced, and air is accelerated. Finally, the presence of the structure does not change the main frequency of ventilated cavity shedding at the front of the structure.

In this paper, the cavity flow of an axisymmetric body under the influence of a structure has been studied, and some results have been obtained, but there are still some problems to be solved. In future research, we will improve the computational fluid dynamics (CFD) model and consider the relative motion between the structure and the axisymmetric body.

ACKNOWLEDGMENTS

This work was supported by the National Natural Science Foundation of China (Nos. 52071062 and 52192692), the Dalian High-level Talent Innovation Support Program (Youth Technology Star) (No. 2020RQ003), the Natural Science Foundation of Liaoning Province of China (No. 2020MS106), the Liao Ning Revitalization Talents Program (No. XLYC1908027), and the Fundamental Research Funds for the Central Universities (Nos. DUT21LK25, DUT20TD108, and DUT20LAB308).

AUTHOR DECLARATIONS

Conflict of Interest

The authors have no conflicts to disclose.

Author Contributions

Di Zhang: Data curation (equal); Formal analysis (equal); Investigation (equal); Methodology (equal); Software (equal); Validation (equal); Visualization (equal); Writing – original draft (equal); Writing – review & editing (equal). **Jianyu Zhang:** Conceptualization (equal); Formal analysis (equal); Investigation (equal); Methodology (equal); Resources (equal); Software (equal); Validation (equal); Visualization (equal); Writing – original draft (equal); Writing – review & editing (equal). **Tiezhi Sun:** Conceptualization (equal); Data curation (equal); Formal analysis (equal); Funding acquisition (equal); Methodology (equal); Project administration (equal); Resources (equal); Supervision (equal); Writing – review & editing (equal). **Yichen Jiang:** Conceptualization (equal); Formal analysis (equal); Investigation (equal); Methodology (equal); Resources (equal); Writing – review & editing (equal).

DATA AVAILABILITY

The data that support the findings of this study are available from the corresponding author upon reasonable request.

REFERENCES

- C. Xu, J. Huang, Y. Wang, X. Wu, C. Huang, and X. Wu, "Supercavitating flow around high-speed underwater projectile near free surface induced by air entrainment," *AIP Adv.* **8**(3), 035016 (2018).
- O. Faltinsen, "Hydrodynamics of high speed marine vehicles," in *Proceedings of the Hydrodynamics VI: Theory and Applications: The 6th International Conference on Hydrodynamics, Perth, Western Australia, 24–26 November 2004* (CRC Press, 2004), p. 3.
- T. Sun, Y. Ding, H. Huang, B. Xie, and G. Zhang, "Numerical study on the effects of modulated ventilation on unsteady cavity dynamics and noise patterns," *Phys. Fluids* **33**(12), 123307 (2021).
- Y. Liu, B. Huang, H. Zhang, Q. Wu, and G. Wang, "Experimental investigation into fluid–structure interaction of cavitating flow," *Phys. Fluids* **33**(9), 093307 (2021).
- R. A. Furness and S. P. Hutton, "Experimental and theoretical studies of two-dimensional fixed-type cavities," *J. Fluids Eng.* **97**(4), 515–521 (1975).
- S. Shao, Y. Wu, J. Haynes, R. E. Arndt, and J. Hong, "Investigation into the behaviors of ventilated supercavities in unsteady flow," *Phys. Fluids* **30**(5), 052102 (2018).
- T. Sun, Z. Wang, L. Zou, and H. Wang, "Numerical investigation of positive effects of ventilated cavitation around a NACA 66 hydrofoil," *Ocean Eng.* **197**, 106831 (2020).
- T. Sun, J. Zhang, X. Zhang, and Y. Jiang, "Study on the influence of temperature on the temporal and spatial distribution characteristics of natural cavitating flow around a vehicle," *J. Mar. Sci. Eng.* **9**(1), 24 (2020).
- T. Sun, X. Zhang, J. Zhang, and C. Wang, "Experimental study on the unsteady natural cloud cavities: Influence of cavitation number on cavity evolution and pressure pulsations," *J. Mar. Sci. Eng.* **9**(5), 487 (2021).
- Y. Jiang, S. W. Jeong, B. K. Ahn, H. T. Kim, and Y. R. Jung, "Experimental investigation of drag characteristics of ventilated supercavitating vehicles with different body shapes," *Phys. Fluids* **31**(5), 052106 (2019).
- S. L. Ceccio, "Friction drag reduction of external flows with bubble and gas injection," *Annu. Rev. Fluid Mech.* **42**, 183–203 (2010).
- W. Zou, T. Liu, Y. Shi, and J. Wang, "Analysis of motion characteristics of a controllable ventilated supercavitating vehicle under accelerations," *J. Fluids Eng.* **143**(11), 111204 (2021).
- A. Karn, R. E. Arndt, and J. Hong, "An experimental investigation into supercavity closure mechanisms," *J. Fluid Mech.* **789**, 259–284 (2016).
- T. Sun, X. Zhang, C. Xu, G. Zhang, C. Wang, and Z. Zong, "Experimental investigation on the cavity evolution and dynamics with special emphasis on the development stage of ventilated partial cavitating flow," *Ocean Eng.* **187**, 106140 (2019).
- T. Sun, X. Zhang, C. Xu, G. Zhang, S. Jiang, and Z. Zong, "Numerical modeling and simulation of the shedding mechanism and vortex structures at the development stage of ventilated partial cavitating flows," *Eur. J. Mech.-B/Fluids* **76**, 223–232 (2019).
- T. Sun, Y. Ding, Y. Liu, and L. Zou, "Numerical modeling and investigation of the effect of internal waves on the dynamic behavior of an asymmetric ventilated supercavity," *Ocean Eng.* **233**, 109193 (2021).
- A. G. Khan, Q. Hisette, H. Streckwall, and P. Liu, "Numerical investigation of propeller-ice interaction effects," *Ocean Eng.* **216**, 107716 (2020).
- P. Xu, C. Wang, L. Ye, C. Guo, W. Xiong, and S. Wu, "Cavitation and induced excitation force of ice-class propeller blocked by ice," *J. Mar. Sci. Eng.* **9**(6), 674 (2021).
- J. Hellmann, K. Rupp, and W. Kuehnlein, "Model tests: LNG-carriers in ice," in *Proceedings of the 25th International Conference on Offshore Mechanics and Arctic Engineering* (ASME, 2006), Vol. 2, pp. 783–789.
- A. V. Pogorelova, V. M. Kozin, and V. L. Zemlyak, "Motion of a slender body in a fluid under a floating plate," *J. Appl. Mech. Tech. Phys.* **53**(1), 27–37 (2012).
- A. V. Pogorelova, V. L. Zemlyak, and V. M. Kozin, "Moving of a submarine under an ice cover in fluid of finite depth," *J. Hydrodyn.* **31**, 562–569 (2019).
- V. L. Zemlyak, A. V. Pogorelova, and V. M. Kozin, "Influence of peculiarities of the form of a submarine vessel on the efficiency of breaking ice cover," paper presented at the Twenty-Third International Offshore and Polar Engineering Conference, Anchorage, Alaska, June 2013.
- V. L. Zemlyak, V. M. Kozin, N. O. Baurin, K. I. Ipatov, and M. V. Kandelya, "The study of the impact of ice conditions on the possibility of the submarine vessels surfacing in the ice cove," *J. Phys.: Conf. Ser.* **919**(1), 012004 (2017).
- V. L. Zemlyak, V. M. Kozin, and N. O. Baurin, "Influence of peculiarities of the form of a submerged body on the parameters of generated waves in the ice motion," *IOP Conf. Ser.: Earth Environ. Sci.* **193**(1), 012024 (2018).
- J. Blake, P. Robinson, A. Shima, and Y. Tomita, "Interaction of two cavitation bubbles with a rigid boundary," *J. Fluid Mech.* **255**, 707–721 (1993).

- ²⁶P. C. Chan, K. K. Kan, and J. H. Stuhmiller, "A computational study of bubble-structure interaction," *J. Fluids Eng.* **122**(4), 783–790 (2000).
- ²⁷P. Cui, A. Zhang, S. Wang, and Y. Liu, "Experimental study on interaction, shock wave emission and ice breaking of two collapsing bubbles," *J. Fluid Mech.* **897**, A25 (2020).
- ²⁸C. A. Brebbia and L. C. Wrobel, "Boundary element method for fluid flow," *Adv. Water Resour.* **2**, 83–89 (1979).
- ²⁹G. V. Logvinovich, *Hydrodynamics of Flows with Free Boundaries*, (IPST, Kyiv, 1969).
- ³⁰C. W. Hirt and B. D. Nichols, "Volume of fluid (VOF) method for the dynamics of free boundaries," *J. Comput. Phys.* **39**(1), 201–225 (1981).
- ³¹C. W. Hirt, A. A. Amsden, and J. L. Cook, "An arbitrary Lagrangian-Eulerian computing method for all flow speeds," *J. Comput. Phys.* **14**(3), 227–253 (1974).
- ³²M. Passandideh-Fard and E. Roohi, "Transient simulations of cavitating flows using a modified volume-of-fluid (VOF) technique," *Int. J. Comput. Fluid Dyn.* **22**(1–2), 97–114 (2008).
- ³³M. A. Fronzo, M. Kinzel, and J. Lindau, "Artificially ventilated cavities: Evaluating the constant-pressure approximation," in *Proceedings of the Fluids Engineering Division Summer Meeting* (ASME, 2017), Vol. 58059, p. V01BT11A022.
- ³⁴N. Gui, L. Ge, P. Cheng, X. Yang, J. Tu, and S. Jiang, "Comparative assessment and analysis of vorticity by Rortex in swirling jets," *J. Hydrodyn.* **31**(5), 495 (2019).
- ³⁵T. Dong, G. Minelli, J. Wang, X. Liang, and S. Krajnović, "Numerical investigation of a high-speed train underbody flows: Studying flow structures through large-eddy simulation and assessment of steady and unsteady Reynolds-averaged Navier–Stokes and improved delayed detached eddy simulation performance," *Phys. Fluids* **34**(1), 015126 (2022).
- ³⁶C. Mockett, *A Comprehensive Study of Detached Eddy Simulation* (Univerlag tuberlin, 2009).
- ³⁷A. Lungu, "Large flow separations around a generic submarine in static drift motion resolved by various turbulence closure models," *J. Mar. Sci. Eng.* **10**(2), 198 (2022).
- ³⁸X. Zhang, C. Wang, Y. Wei, and T. Sun, "Experimental investigation of unsteady characteristics of ventilated cavitation flow around an under-water vehicle," *Adv. Mech. Eng.* **8**(11), 1–9 (2016).
- ³⁹J. Zhou, K. Yu, J. Min, and Y. Ming, "The comparative study of ventilated super cavity shape in water tunnel and infinite flow field," *J. Hydrodyn., Ser. B* **22**(5), 689–696 (2010).
- ⁴⁰L. Cao, A. Karn, R. Arndt, Z. Wang, and J. Hong, "Numerical investigations of pressure distribution inside a ventilated supercavity," *J. Fluids Eng.* **139**(2), 021301 (2017).
- ⁴¹Y. Choe and C. Kim, "Computational investigation on ventilated supercavitating flows and its hydrodynamic characteristics around a high-speed underwater vehicle," *Ocean Eng.* **249**, 110865 (2022).
- ⁴²S. Gaggero, D. Villa, and S. Brizzolara, "RANS and PANEL method for unsteady flow propeller analysis," *J. Hydrodyn., Ser. B* **22**(5), 547–569 (2010).
- ⁴³Y. Zhang, K. Chen, and D. Jiang, "CFD analysis of the lateral loads of a propeller in oblique flow," *Ocean Eng.* **202**, 107153 (2020).
- ⁴⁴J. Gong, Z. Wu, J. Ding, J. Jiang, and Z. Zhang, "Numerical analysis of propulsion performance of a waterjet-propelled vehicle in steady drift," *Ocean Eng.* **266**, 113136 (2022).
- ⁴⁵C. Liu, Y. Wang, Y. Yang, and Z. Duan, "New Omega vortex identification method," *Sci. China: Phys., Mech. Astron.* **59**(8), 1–9 (2016).
- ⁴⁶X. Dong, Y. Wang, X. Chen, Y. Dong, Y. Zhang, and C. Liu, "Determination of epsilon for Omega vortex identification method," *J. Hydrodyn.* **30**(4), 541–548 (2018).
- ⁴⁷C. Liu, Y. Gao, S. Tian, and X. Dong, "Rortex—A new vortex vector definition and vorticity tensor and vector decompositions," *Phys. Fluids* **30**(3), 035103 (2018).
- ⁴⁸A. May, "Water entry and the cavity-running behavior of missiles," Navsea Hydroballistics Advisory Committee Silver Spring MD Report No. ADA020429, 1975.